# European summer weather linked to North Atlantic freshwater anomalies in preceding years

Marilena Oltmanns[1], N. Penny Holliday[1], James Screen[2], Ben I. Moat[1], Simon A. Josey[1], D. Gwyn Evans[1], and Sheldon Bacon[1]

[1]National Oceanography Centre, Southampton, UK
[2]University of Exeter, Exeter, UK

**Correspondence:** Marilena Oltmanns (marilena.oltmanns@noc.ac.uk)

**Abstract.** Amplified Arctic ice loss in recent decades has been linked to increased occurrence of extreme mid-latitude weather. The underlying mechanisms remain elusive, however. One potential link occurs through the ocean as the loss of sea ice and glacial ice leads to increased freshwater fluxes into the North Atlantic. Thus, in this study, we examine the link between North Atlantic freshwater anomalies and European summer weather. Combining a comprehensive set of observational products, we show that stronger freshwater anomalies are associated with a sharper sea surface temperature front between the subpolar and the subtropical North Atlantic in winter, an increased atmospheric instability above the sea surface temperature front, and a large-scale atmospheric circulation that induces a northward shift in the North Atlantic Current, shifting and strengthening the sea surface temperature front. In the following summer, the jet stream is deflected along the enhanced sea surface temperature front and the European coastline, leading to warmer and drier weather over Europe. Accordingly, we find that stronger freshwater anomalies in the subpolar North Atlantic in winter are followed by warmer and drier weather over Europe in the subsequent summer, with the regions of the warm and dry anomalies being sensitive to the location, strength and extent of the North Atlantic freshwater anomalies in the preceding winter. The identified statistical links are significant on timescales from years to decades and indicate an enhanced predictability of European summer weather several months in advance.

## 1 Introduction

Arctic near-surface temperature is currently warming twice as fast as the global average (Cohen et al., 2019), which manifests itself in an average sea ice volume loss of $3.0 \pm 0.2 \cdot 1000 \text{ km}^3 \text{ decade}^{-1}$, based on the period 1979 to 2018 (Kumar et al., 2020). Similarly large losses are observed for land ice, particularly from the Greenland ice sheet, amounting to $3.0 \pm 0.3 \cdot 1000 \text{ km}^3 \text{ decade}^{-1}$, based on the period 2003 to 2012 (Khan et al., 2015). Earlier studies noticed statistical links between an amplified sea ice loss at high latitudes and an increased occurrence of weather extremes at mid-latitudes (Francis and Vavrus, 2012; Tang et al., 2014; Screen and Simmonds, 2013; Cohen et al., 2014). However, the robustness of these links has been questioned and the underlying mechanisms are poorly understood (Barnes, 2013; Overland et al., 2015; Blackport and Screen, 2020).

One potential connection occurs through the ocean. Specifically, the loss of sea ice and glacial ice in the Arctic and sub-Arctic regions constitutes a source of freshwater for the North Atlantic (Bamber et al., 2018; Carmack et al., 2016). Large North Atlantic freshwater anomalies, moreover, were found to give rise to cold surface anomalies and the development of storms in the subpolar region in winter (Oltmanns et al., 2020). In turn, cold anomalies in the subpolar region in winter were found to precede heat waves over Europe in the subsequent summer (Duchez et al., 2016; Mecking et al., 2019). The heat waves were attributed to a stationary jet stream over the North Atlantic (Duchez et al., 2016) and were successfully reproduced in model simulations initialised with the cold anomaly (Mecking et al., 2019). Thus, by triggering cold anomalies in winter, increased surface freshening could initiate a deterministic chain of events that first leads to cold anomalies and storms in winter and then heat waves in the subsequent summer.

While earlier studies support individual connections between the North Atlantic sea surface temperature (SST) and the jet stream (Woollings et al., 2010), or between shifts in the jet stream and European heat waves (Dong et al., 2013; Gervais et al., 2020), the role of freshwater in initiating this causal chain is unclear. Yet, given that the Arctic and sub-Arctic regions are expected to continue to warm and release freshwater from melting sea ice and glacial ice into the North Atlantic, it is critical to understand how the resulting feedbacks will affect weather in Europe.

The gap in our knowledge around the potential influences of North Atlantic freshwater anomalies on European summer weather arises from the difficulty to simulate salinity. Freshwater enters the subpolar region through narrow boundary currents and mesoscale eddies requiring a fine grid spacing of $\sim 1/12°$ (Marzocchi et al., 2015; Böning et al., 2016; Müller et al., 2019). Most current coupled global climate models have a coarser grid spacing, giving rise to salinity biases (Mecking et al., 2017; Menary et al., 2015; Wu et al., 2018). From an observational perspective, estimating freshwater variations is also difficult. In-situ observations of sea surface salinity mostly stem from Argo floats which cannot fully capture the large spatial variability at high temporal resolution. Moreover, satellite observations of sea surface salinity are associated with large uncertainties and only available since 2009 (Bao et al., 2019; Xie et al., 2019).

Given the limitations associated with currently available model and observational products of sea surface salinity, we use a new approach to estimate freshwater variations, taking advantage of a dynamical constraint of the sea surface salinity on the SST. In the subpolar region in autumn and winter, the air is colder than the ocean surface. Thus, the surface water is cooled by the atmosphere, becomes denser, and sinks. Enhanced surface freshening reduces the surface density and requires additional cooling before the surface water is dense enough to sink. This constraint of freshwater on the surface cooling can be used to infer its variability using a mass balance analysis (Oltmanns et al., 2020).

In the following, we describe the involved data products (Section 2). We then explain the approach to estimate freshwater variability from a surface mass balance (Section 3). In Section 4, we examine the ocean-atmosphere evolution associated with freshwater anomalies, and assess their links with European summer weather based on statistical analyses (Section 4). We conclude by discussing the dynamical role of freshwater anomalies in the identified ocean-atmosphere evolution and the implications for predictability (Section 5).

## 2 Data

First, we describe the observational products involved in this study and describe any processing steps. Since the analyses are based on statistical methods, a high data quality is important. Thus, we focussed on the period since 1979, motivated by the increased data quality associated with the onset of satellite observations in 1979.

### 2.1 Datasets

The analysis of ocean variability includes a merged SST product consisting of Hadley Centre HadISST1 data (Rayner et al., 2003; Hurrell et al., 2008) and optimal-interpolated, remote sensing-based SST data from NOAA (Reynolds et al., 2002). The merged Hadley – NOAA data product has a monthly temporal resolution, a $1°$ x $1°$ spatial resolution and is available from https://gdex.ucar.edu/dataset/158_asphilli.html.

To assess changes in surface currents, we further used absolute dynamic topography data since 1993, derived from altimetry (Le Traon et al., 1998). Absolute dynamic topography represents the sea level anomaly with respect to the geoid and thus, the stream function of the geostrophic surface flow. The monthly, gridded, absolute dynamic topography dataset has a spatial resolution of $0.25°$ x $0.25°$ and is distributed by the Copernicus Marine Environment Monitoring Service (https://marine.copernicus.eu/). Geostrophic surface velocities were calculated from the absolute dynamic topography using $u_g = -\frac{g}{f R_E} \frac{\partial \eta}{\partial \theta}$ and $v_g = \frac{g}{f R_E cos(\theta)} \frac{\partial \eta}{\partial \phi}$, where $u_g$ and $v_g$ are the zonal and meridional velocities, $\eta$ is the absolute dynamic topography, $g$ is the gravitational acceleration, $f$ is the Coriolis parameter, $R_E$ is the Earth's radius, and $\theta$ and $\phi$ are the latitude and longitude respectively.

Moreover, to compare freshwater anomalies, estimated from the surface mass balance analysis, with in-situ observations from the subpolar North Atlantic, we included a hydrographic, mixed layer database. The dataset provides mixed layer depths, mixed layer salinities, and mixed layer temperatures, derived from Argo float profiles (Holte et al., 2017). It is freely available at http://mixedlayer.ucsd.edu.

The ocean data is complemented by monthly output from the ERA5 atmospheric reanalysis model from the European Centre for Medium-Range Weather Forecasts since 1979 (Hersbach et al., 2018). In addition to the standard variables from ERA5, we estimated the maximum Eady growth rate. The maximum Eady growth rate is used to assess the baroclinic instability in the atmosphere over increased meridional SST gradients. Following earlier studies (Lindzen and Farrell, 1980; Dierer et al., 2005), we estimated the maximum Eady growth rate in the 1000 hPa to 750 hPa layer with $\sigma_E \approx 0.31 \frac{f}{N} \mid \frac{u_{750} - u_{1000}}{z_{750} - z_{1000}} \mid$, where $f$ is again the Coriolis frequency, $u$ is the zonal wind, $z$ the height, $N$ the Brunt-Väisälä frequency and the subscripts refer to the associated pressure levels.

A key parameter, used to derive freshwater indices, is the mean North Atlantic Oscillation (NAO), obtained from the National Oceanic and Atmospheric Administration (NOAA) Climate Prediction Center. The NAO index was calculated using Rotated Principal Component Analysis, applied to the monthly standardised 500 hPa geopotential height anomalies between $20°N$ and $90°N$ (Barnston and Livezey, 1987) and identified as the dominant mode of variability in the northern hemisphere. A detailed derivation can be found at https://www.cpc.ncep.noaa.gov/products/precip/CWlink/pna/nao.shtml.

Lastly, we included data from the Greenland climate model MAR to assess potential causes of freshwater anomalies. We used version 3.12, run at a resolution of 20 km forced by the ERA5 reanalysis (Fettweis et al., 2017) and distributed by the Laboratory of Climatology at the University of Liège. For the purpose of this study, we considered the runoff over the full ice sheet from 1950 through to the end of 2022 at monthly resolution. The dataset is available at ftp://ftp.climato.be/fettweis/MARv3.12.

## 2.2 Preprocessing

Over the investigated period, the climate has been characterised by increasing greenhouse gas concentrations, leading to enhanced surface warming (Lashof and Ahuja, 1990). Over the last two decades, moreover, the freshening has also been increasing (Tesdal et al., 2018), particularly because of increased runoff and melting from Greenland (Bamber et al., 2012, 2018). Thus, the surface warming resulting from increased greenhouse gases could superimpose on potential surface cooling or warming signals resulting from changes in the ocean or atmospheric circulations associated with increased North Atlantic surface freshening. This superposition could distort the interpretation of the statistical analyses when assessing the specific influences of changes in the ocean and atmospheric circulations associated with increased North Atlantic freshening.

Considering that the freshening trend is an important part of the signal we are investigating, removing trends at each location (or grid point) would remove an important part of a signal that we are interested in. Thus, to reduce the influence of increasing greenhouse gas concentrations on European air temperatures, we subtract regionally averaged trends from the air temperature. The method of subtracting regionally averaged trends is motivated by the observation that greenhouse gases are distributed comparatively uniformly in the atmosphere (Reuter et al., 2020) whereas the observed surface warming exhibits large regional differences (Simmons, 2022). These regional differences in surface warming result from changes in the ocean and atmospheric circulations, which are redistributing the exess heat. Since, in this study, we are specifically interested in these dynamic processes associated with changes in the ocean and atmospheric circulations, we are subtracting a spatially uniform warming trend associated with increasing greenhouse gases.

We tested different regions and found that the results are not sensitive to the exact area that is used for the averaging, as long as it is sufficiently large. Here, we averaged over the main area of investigation from 25 °N to 65 °N and from 60 °W to 60 °E, resulting in an average trend of ∼0.04 °C year$^{-1}$ in the 2-m air temperature from ERA5. Extending the region in any direction does not appreciably change this trend, nor the subsequent results, consistent with the assumption that the direct warming trend that is solely due to increasing greenhouse gases is distributed relatively uniformly.

While the summer air temperature is strongly affected by a spatially uniform warming trend, the other variables exhibit no or only minor trends after they have been averaged over a large area. Thus, after removing the trend in the air temperature prior to the analyses, we obtain a signal that is dynamically consistent across all investigated variables. If, on the other hand, we do not remove the trend in the air temperature, we still obtain the same patterns throughout the results but there would be a large-scale, uniform warming signal superimposed over the full domain.

We did not apply any other averaging, smoothing, filtering, or further preprocessing steps to the datasets.

## 3 Estimation of freshwater anomalies

The objective of this study is to investigate feedbacks initiated by freshwater anomalies. However, high-quality global salinity measurements have only been routinely available since 2002, and mostly in the open ocean from Argo floats. Moreover, satellite observations of the sea surface salinity are of relatively low accuracy and only available since 2009 (Bao et al., 2019; Xie et al., 2019). Considering the limitations associated with currently available salinity products, we use a surface mass balance analysis to estimate the variability of freshwater.

### 3.1 Mass balance

The mass budget for the surface mixed layer in the subpolar region in winter can be expressed as:

$$\frac{\partial}{\partial t} \left( \int_{-h(t)}^{\eta} \rho \, dz \right) = -\frac{B}{g} - \nabla \cdot \left( \int_{-h(t)}^{\eta} \rho \boldsymbol{u} \, dz \right), \tag{1}$$

where $\rho$ is the mixed layer density, $h$ is the mixed layer depth, $\eta$ is the surface elevation above the geoid (which is equivalent to the absolute dynamic topography), $g$ is the gravitational acceleration, $B$ is the buoyancy flux through the surface, and $\boldsymbol{u}$ corresponds to the velocity vector (Gill, 2016; Griffies and Greatbatch, 2012). The term $-\nabla \cdot \left( \int_{-h(t)}^{\eta} \rho \boldsymbol{u} \, dz \right)$ represents the convergence of mass, which we separate into an active component $A$ and a passive component $E$. The passive component is defined as the entrainment of mass into the mixed layer that results from mixed layer deepening as the mixed layer density increases. The active component results from externally forced, horizontal and vertical mass fluxes, such as wind-driven Ekman transports and upwelling. The passive component can only change the mixed layer depth, but not its density, while the active component does change the mixed layer density.

Next, we assume that the density is homogeneous in the mixed layer and that $\eta$ in winter is much smaller than the mixed layer depth $h$. After integrating Eq. (1) from summer to winter and neglecting the contribution of the surface elevation $\eta$ relative to the mixed layer depth on the lefthand side of Eq. (1), we thus obtain:

$$\rho h \approx h_0 \rho_0 + \left( -\frac{B}{g} + A + E \right) \cdot \Delta t, \tag{2}$$

where $h_0$ and $\rho_0$ represent a mixed layer depth and density at the end of the summer (for instance in September), $h$ and $\rho$ refer to the depth and density in winter (January to March), and $\Delta t$ is the corresponding integration interval from summer to winter.

While the climatological mean mixed layer density increases during the winter, the mixed layer deepens. Thus, before the winter, the mixed layer is several tens of metres deep while during the winter, it reaches several hundred metres. Since the density anomaly in the initial shallow mixed layer becomes distributed over a much larger depth range, the first term on the righthand side is negligible compared to the other terms. Any density anomalies beneath the initial, shallow mixed layer are still included in $E$. Eq. (2) thus simplifies to:

$$\rho h \approx \left( -\frac{B}{g} + A + E \right) \cdot \Delta t. \tag{3}$$

We further separate each term into a mean and an anomaly $n$, with $n$ referring to the n'th winter of an arbitrary subset of $N$ winters and the mean representing the mean over these winters. Since we have defined $E$ as a passive component that can only change the mixed layer depth, not its density, we can write it as $E_n \cdot \Delta t = h_n \cdot (\rho_n + \rho_{mean})$. Moreover, assuming that the mean state is in balance, we subtract the mean values from Eq. (3), resulting in:

$$\rho_n h_{mean} + \rho_{mean} h_n + \rho_n h_n \approx \left( -\frac{B_n}{g} + A_n \right) \cdot \Delta t + h_n \cdot (\rho_n + \rho_{mean}), \tag{4}$$

where the terms involving $h_n$ cancel each other.

Lastly, we express the density as a function of temperature and salinity by considering variations in the density around a reference, which we choose to be the mean over the $N$ selected winters. Since local density variations due to pressure are several orders of magnitude smaller than those, due to changes in salinity and temperature (Talley, 2011), we only consider temperature and salinity variations: $\rho_n \approx \rho_{mean} (-\alpha \cdot T_n + \beta \cdot S_n)$, where $T$ is the temperature, $S$ is the salinity, $\alpha$ and $\beta$ are the thermal and haline expansion coefficients. Plugging this expression into Eq. (4), we obtain:

$$\rho_{mean} (-\alpha \cdot T_n + \beta \cdot S_n) \cdot h_{mean} \approx \left( -\frac{B_n}{g} + A_n \right) \cdot \Delta t. \tag{5}$$

The objective of the following analysis is to find conditions in which the density anomalies associated with temperature anomalies are much larger than the effect of potential, active drivers of density anomalies on the righthand side of Eq. (5): $\rho_{mean} \cdot h_{mean} \cdot |\alpha \cdot T_n| \gg |\left( -\frac{B_n}{g} + A_n \right)| \cdot \Delta t$. Under these conditions, the temperature and salinity anomalies must compensate each other in their influence on density, allowing us to estimate the salinity anomalies from the associated temperature anomalies: $\beta S_n \approx \alpha T_n$.

The idea that such conditions exist is motivated by the observation that salinity changes are not only a response to surface fluxes and entrainment but can, in turn, constrain the drivers of density anomalies. Large freshwater anomalies in winter can impede convection and entrainment and thus limit the oceanic heat release to the atmosphere ($B$). At the same time, a stronger surface cooling is required to mix freshwater down, influencing the mixed layer temperature $T$. Considering the competing influences of salinity and temperature on stratification, the conditions in which freshwater may impact the temperature, can only occur in autumn and winter, when surface water is cooled by the atmosphere, becomes denser and sinks. In summer, the temperature and salinity do not compete in their influence on stratification and thus, do not constrain each other.

To exploit this constraint of salinity on temperature and identify these potential conditions, we assume that the surface mixed layer in winter is relatively well mixed, so we can approximate the mixed layer temperature $T$ with the SST. We then search for potential freshwater indices that exhibit a strong linear relationship with subpolar SST anomalies, regress Eq. (5) onto these indices, and compare the magnitude and spatial characteristics of the resulting terms. If enhanced surface freshening substantially affected the SST, we expect the terms $A_n$ and $B_n$ to drop out of Eq. (5) after the regression. In essence, the indices serve as filters that help us to identify conditions in which freshwater anomalies have been sufficiently large to influence the heat exchange between the ocean and the atmosphere, either within the subpolar region or before entering it. Later (in Section 4.5), we will further assess if these conditions in which the air-sea heat exchange and in turn the SST have been affected by freshwater anomalies hold generally over the North Atlantic or only for selected indices.

## 3.2 Derivation of freshwater indices

The challenge in detecting the conditions in which freshwater anomalies may have affected the SST, consists in the complexity of SST and freshwater variability in the subpolar region. In theory, changes in surface freshwater can be influenced by river runoff, sea ice and glacial melting, evaporation and precipitation, mixing, and ocean currents. Considering that multiple factors can contribute to freshwater variations over a range of timescales and spatial scales, it may not be possible to reduce the complexity of freshwater variability in space and time into a single, one-dimensional index.

To overcome this challenge, we construct indices over subsets of years that allow us to closely constrain the variability of the SST, over the selected subset. Thus, this approach is different to traditional methods in which the dynamical mechanisms are known a priori, and statistical methods are used to assess the significance of these mechanisms. Here, we first select indices with a strong and significant statistical relationship with the SST, and then look for potential freshening mechanisms that can explain the relationship, assuming that these mechanisms exist but may be masked by other drivers.

As a first, educated guess to identify suitable freshwater indices, we start with the NAO index in summer, motivated by its dynamical links to freshwater. On the one hand, a lower NAO phase in summer has been associated with enhanced runoff and melting over Greenland (Hanna et al., 2013, 2021), which is a source of freshwater to the North Atlantic (Bamber et al., 2018; Dukhovskoy et al., 2019). On the other hand, a higher NAO phase has been associated with an intensified subpolar gyre circulation, leading to enhanced freshwater imports into the subpolar region (Häkkinen et al., 2011a, 2013; Holliday et al., 2020). Yet, even if the freshening occurs in summer (when melting and runoff is strongest), the effect of the freshwater on the SST would only become visible in autumn and winter (when the freshwater impedes the sinking of surface water). Thus, we focus on the SST in winter to infer the possible existence of freshwater anomalies.

Consistent with the existence of multiple possible drivers of freshwater and SST anomalies in winter, we obtain a qualitatively different relationship between the summer NAO index in July and August ($NAO_S$) and the temperature difference between the subpolar and subtropical gyres in the subsequent winter below and above a threshold of $\sim -0.5$ in $NAO_S$ (Fig. 1a and b). Below this threshold, there is a progressively larger SST difference between the northern subtropical region and the southern subpolar region for decreasing $NAO_S$ phases in the preceding summer (Fig. 1a). Above this threshold, there is a progressively larger SST difference for increasing $NAO_S$ phases in the preceding summer. Also, the associated cold, subpolar SST anomaly is weaker and displaced further to the northwest (Fig. 1b).

Next, we strengthen the identified relationships between the two NAO subsets (above and below $-0.5$) and the subsequent SST anomalies through subsampling. Specifically, if $x_i$ corresponds to the $NAO_S$ subset years, and $y_i$ corresponds to the SST anomaly in the subsequent winter, we strive to derive a linear relationship $y = ax + b$, where $a$ and $b$ are constants and in which $|a|$ is high. The higher the magnitude of $a$ is, the higher is the magnitude of $\alpha T$ on the lefthand side of Eq. (5) after regressing Eq. (5) onto the index. Thus, we aim to select NAO years for which the magnitude of the slope $a = \frac{y_i - y}{x_i - x_0}$ is large, where $x_0 = x|_{y = \bar{y}_i}$ and $\bar{y}_i$ represents the mean over $y_i$. At the same time, we strive to obtain a high correlation between the subset and the subsequent SST anomalies. Thus, we aim to select NAO years where $(x_i - x_0)^2$ is large, since this increases the variance of the SST anomalies that can be explained by the index.
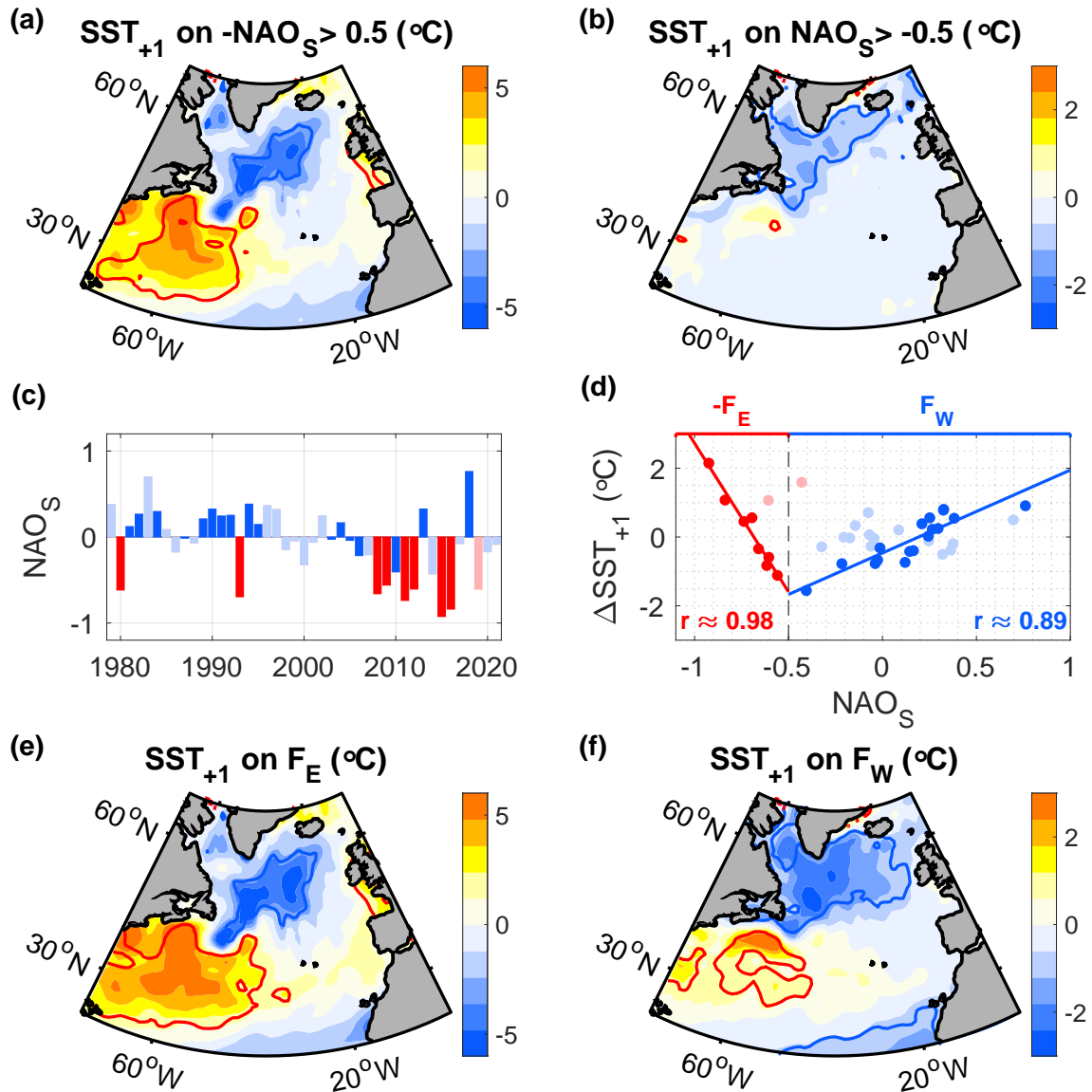
**Figure 1.** (a,b) Regression of the SST in winter (January through to March) onto (a) $-\mathrm{NAO}_S$ in all years in which $\mathrm{NAO}_S < -0.5$ and (b) $+\mathrm{NAO}_S$ in all years in which $\mathrm{NAO}_S > -0.5$, where $\mathrm{NAO}_S$ refers so the NAO index of the preceding summer (July and August). The '+1' in the title refers to the time lag of the SST signal since it appears in the winter after the summer index. (c) Variability of the NAO index in July and August ($\mathrm{NAO}_S$), with the colour coding matching that in d. (d) Relationship between $\mathrm{NAO}_S$ and the subsequent winter SST, where $\Delta$SST corresponds to the SST difference between the red, subtropical and blue, subpolar 95% confidence regions in panels e (red years) and f (blue years) respectively, relative to the respective means. (e,f) Regression of the SST in winter onto the two freshwater indices, obtained after the subsampling. The corresponding years are shown by the strong red and blue colours in panels c and d, excluding the faint years. Thus, $F_E$ includes 8 years while the regression on $F_W$ is based on 17 years. Contours encompass regions that are significant at the 95% confidence level. Please note the different colour scales.

The values $x_i$ included in each subset directly correspond to the respective $NAO_S$ values (Fig. 1c) without scaling them, while the values $y_i$ correspond to the SST difference between the subpolar and the subtropical gyres, rather than only the SST anomaly at a single location. Using the SST difference has the advantage that we filter out any spatially uniform, radiative warming signals due to increasing greenhouse gas concentration and base the analysis on larger regions. In addition, we only consider regions in which the SST anomalies are significant, allowing us to directly inspect the robustness of the underlying correlations and ensure that they are not due to outliers or clusters. Thus, we identified two outliers, corresponding to the NAO summers in 2014 and 2019 (faint red years in Figure 1d), which we excluded from the subsequent subsampling to obtain a faster convergence of the results.

Following the above objectives to maximise the slope and variance of the subsampled index, we select the $N$ years where the term $(y_i - y) \cdot (x_i - x_0)$ is highest. Here, the subscript $i$ refers to all years in the two sets where the $NAO_S$ is above or below 0.5 respectively, excluding the two outliers, and $y$ is the associated, linear regression of $y_i$ on $x_i$. Graphically, the subsampling is equivalent to increasing the slope of the regression line while keeping a high variance (Fig. 1d). It represents a powerful method for increasing the statistical relationship between two variables and thus identifying dynamical links, based on the assumption that noise, and other mechanisms, can mask these links. Once a strong statistical connection has been established, the physical basis will be assessed by investigating the potential, underlying dynamical links.

There is a trade-off between the number of years $N$ included in each subset and the resulting correlations between the NAO subset and subsequent SST pattern. Considering that the number of years is already low for the cold anomalies preceded by strongly negative NAO summers ($N = 8$), where $NAO_S$ is smaller than $-0.5$, we do not apply any further subsampling. For the other subset, we selected $N = 17$ years as a reasonable compromise for obtaining a high correlation of $\sim 0.90$ while keeping a relatively large sample size, reflected in the low p-value of $\sim 1.8 \cdot 10^{-6}$.

In Section 4.5 and Appendix B, we show that the results are not sensitive to the subsampling or the number of years included. However, having a close relationship between the index and the SST results in reduced uncertainties when estimating the associated freshwater anomalies. In addition, the high correlations help us to identify and assess potential dynamical links more clearly: Freshwater indices that are only poorly correlated with freshwater are only of limited use when assessing links between freshwater and other ocean or atmospheric parameters. Since the indices will be used as a tool for representing freshwater anomalies, high correlations between the indices, the SST and potential freshwater anomalies are a prerequisite, not a conclusion, and we make no assumptions on the suitability of both subsets outside the selected years.

Through the subsampling, we have derived two subsets with close, linear relationships with the SST (Fig. 1d, e and f). To distinguish the two subsets from each other, we name them according to the location of the associated cold SST anomalies. Since the maximum cold anomalies associated with lower NAO states ($NAO_S < -0.5$) are strongest over the southeastern subpolar region (Fig. 1e), we refer to the selected 8 years as $F_E$ index — shown by the clear red coloured bars in Figure 1c and listed. For the other subset, the maximum cold anomalies extend over the full subpolar gyre, including the western part (Fig. 1f). Thus, we refer to the selected 17 years as $F_W$ index — shown by the clear blue coloured bars in Figure 1c. The corresponding years included in each index are additionally listed in Table A1. In the following analyses, we will examine the dynamical links of both indices to freshwater anomalies and the associated air-sea feedbacks.

## 4 Results

Having selected two NAO subsets, we will first assess their suitability for representing freshwater anomalies. Thus, we evaluate the associated mass balance to estimate freshwater anomalies and examine their potential causes. We will then use the indices to investigate links between the estimated freshwater anomalies and the large-scale ocean and atmospheric conditions in winter and summer, and test if the identified links hold generally by using an un-subsampled index. Lastly, we will assess the role of North Atlantic freshwater anomalies as a predictor for Europe's warmest summers by constructing composites of the 10 warmest relative to the 10 coldest summers between 1979 and 2022 and comparing the preceding freshwater anomalies.

### 4.1 Estimation of freshwater anomalies

Taking advantage of the strong relationships between the selected $\text{NAO}_S$ subsets and subsequent SST anomalies, we regress each term in Eq. (5) on the corresponding indices $F_E$ and $F_W$. We then evaluate the surface mass balance over the subpolar cold SST anomaly regions within the regions enclosed by the 95% confidence lines. In the following, we present the key analysis steps and results while a detailed evaluation and comparison with in-situ observations is provided in Appendix A.

To estimate the temperature term $\alpha T_n$, we again assume that the mixed layers are relatively homogenous and approximate the mixed layer temperature with the SST, averaged over the winter (January through to March). Even if the SST is slightly warmer or colder than the mixed layer temperature, the relationship between the mixed layer temperature and the mixed layer salinity will still remain the same as that between the SST and the sea surface salinity, due to having a constant density profile in the mixed layer. To estimate the mean mixed layer depth $h_{mean}$, moreover, we averaged the mean mixed layer depth, obtained from Argo floats (Holte et al., 2017), over the same regions and months as the SST, resulting in a mean mixed layer depth of $\sim$250 m for the $F_E$ subset and $\sim$280 m for the $F_W$ subset.

We further compute $\alpha$ and $\beta$ using the Gibbs Seawater Routines (McDougall et al., 2009), in accordance with the highest standards of current knowledge. Noting that the effects of salinity and pressure on $\alpha$ and $\beta$ are small and only affect the second decimal place or less, we use nominal values of 35 g kg$^{-1}$ and 10 db for the subpolar region in winter to compute $\alpha$ and $\beta$. The dependence of $\alpha$ and $\beta$ on temperature is larger, however. For instance, $\alpha$ can vary from $5 \cdot 10^{-4}$ to $18 \cdot 10^{-4}$ °C$^{-1}$ across the subpolar ocean surface. Thus, for an enhanced accuracy, we allow $\alpha$ and $\beta$ to vary with the SST.

Next, we estimate the terms on the righthand side of Eq. (5). On the timescales and spatial scales considered, oceanic flows are predominantly in geostrophic balance, redistributing heat and freshwater. However, geostrophic flows cannot contribute to a net mass input. Over the open ocean, away from topographic boundaries, on interannual timescales, the winds and air-sea fluxes represent the largest energy sources that can result in vertical mixing or horizontal mass convergence (Ferrari and Wunsch, 2009; Wunsch and Ferrari, 2004). Other sources of energy include pressure loading by the atmosphere, geothermal heating, biological activity, and the tides but we estimate them to be negligible over the investigated timescales and spatial scales. Thus, the terms on the righthand side of Eq. (5) are confined to the surface buoyancy fluxes, horizontal Ekman transports and wind-driven vertical fluxes, all of which are estimated using the atmospheric reanalysis ERA5. Considering the nonlinearity within the individual terms of Eq. (5), we first evaluate each term before regressing it onto the indices.

285    After estimating the density anomalies associated with the cold anomalies, and the buoyancy fluxes, the horizontal Ekman transports and the vertical Ekman velocity, and regressing them onto the freshwater indices (Appendix A), we find: Regardless of the exact region and mean mixed layer depth, and regardless of which month is selected as starting month of the integration, the density increase implied by the cold anomalies associated with $F_E$ and $F_W$ is always more than an order of magnitude larger than the density changes associated with $A_n$ or $B_n$. Moreover, neither of these fluxes is significantly correlated with the

290    subsets, and their spatial patterns are inconsistent with the obtained SST patterns, regardless of whether we include the full subpolar region where the SST anomaly is negative or only the region enclosed by the 95% confidence lines, or whether we start the integration in October or only consider the winter months January to March.

With the buoyancy fluxes, vertical Ekman transports and horizontal advection being negligible, we conclude that the density increase associated with the cold anomalies must be balanced by a density decrease associated with freshwater anomalies:

295    $\alpha SST_E \approx \beta SSS_E$, and $\alpha SST_W \approx \beta SSS_W$, where $SSS$ is the sea surface salinity and the subscripts refer to the anomalies obtained from the regressions onto the respective index. This result implies a close connection between freshwater and SST anomalies included in each subset. A demonstration of the connection between SSS and SST anomalies with hydrographic observations shows that, even in winters with most intense air-sea fluxes, freshwater anomalies can still be inferred from the SST with reasonably small uncertainties (Appendix A).

300    Using the obtained density compensation between SSS and SST anomalies, we estimate SSS anomalies from the two NAO subsets. Thus, we find that the maximum freshwater anomalies (or minimum SSS anomalies) associated with $F_E$ occur over the central subpolar region (corresponding to the southeastern subpolar gyre) and are spatially more confined than the maximum freshwater anomalies associated with $F_W$ (Fig. 2a and b). Moreover, the significant area of $F_W$ freshwater anomalies extends further eastward, westward, and northward compared to $F_E$ freshwater anomalies and the anomalies have a smaller amplitude,

305    consistent with the associated cold, subpolar SST anomalies (Fig. 1e and f).

Since the buoyancy fluxes represent the largest term on the righthand side of Eq. (5), they determine the uncertainty of the obtained salinity estimates, amounting to 4% for the $F_E$ subset and 6% for the $F_W$ subset (Appendix A). These uncertainties apply to the cold anomaly regions, enclosed by the 95% lines. Uncertainties at each individual grid point can differ. Moreover, if the freshwater forcing is very large, the surface mass balance may underestimate the freshening because freshwater anomalies

310    can (in theory) increase up to a salinity threshold of zero, while SST anomalies cannot drop below the air temperature. Still, we find that even during the strong observed freshwater anomalies in 2015 and 2016, the surface mass balance provided a good approximation (Appendix A), suggesting that a potential underestimation is only small.

In addition to the low overall uncertainties of the SSS estimates, another implicit advantage of the selected NAO subsets $F_E$ and $F_W$ is that they are, by construction, highly correlated with the obtained freshwater estimates in the subsequent winter,

315    with the magnitude of the correlations between the SSS anomalies and the freshwater indices exceeding 0.9 (Fig. 2c and d). The SSS correlations with the $F_E$ subset reach their highest magnitude over the southeastern subpolar gyre while the highest magnitudes of the SSS correlations with $F_W$ occur over the central and northern subpolar region, covering an overall larger area, like the corresponding regressions. Considering the low uncertainties of the obtained freshwater estimates, and their high correlations with the two NAO subsets, we conclude that both subsets represent suitable freshwater indices.
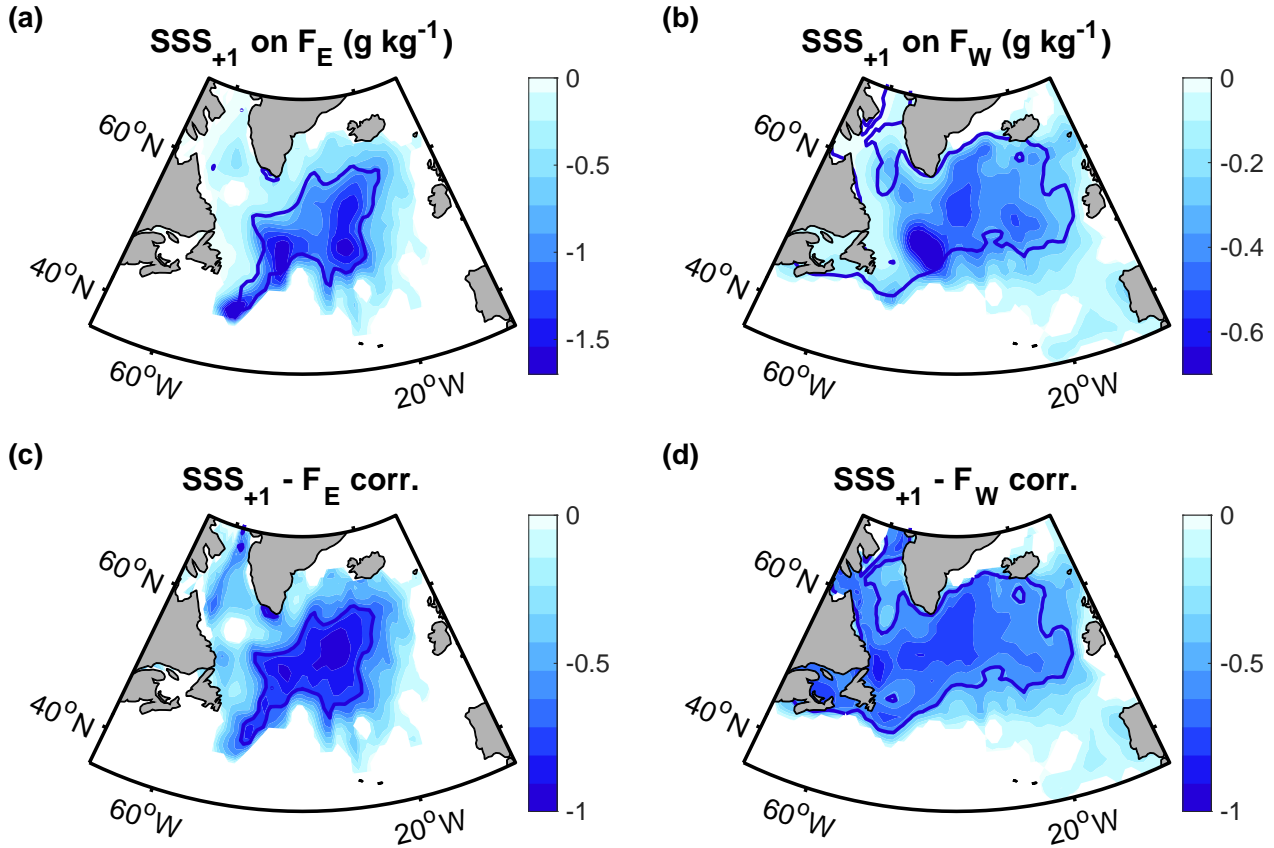
**Figure 2.** (a,b) Regression of the sea surface salinity in winter (January through to March) on the two freshwater indices from the preceding summer (Fig. 1c). The contours delineate the regions that are significant at the 95% confidence level. (c,d) Correlations between the sea surface salinity in winter and the freshwater indices from the preceding summer, with the thick contours delineating the regions that are significant at the 95% confidence level, assessed by means of two-sided t-tests. The underlying sea surface salinity variability has been estimated from the surface mass balance by assuming density compensation with the SST anomalies.

## 4.2 Causes of freshwater anomalies

Freshwater anomalies may result from enhanced sea ice or glacial melt, river runoff, surface fluxes (precipitation minus evaporation), and circulation changes. After investigating the surface fluxes from ERA5, glacial runoff from the Greenland climate model MAR, and the regional gyre circulation from altimetry, we find a significant negative relationship between the summer NAO and runoff (Fig. 3a), pointing to runoff as potential freshwater source for the $F_E$ freshwater anomalies, associated with a strongly negative $NAO_S$ index. While other sources of meltwater, such as sea ice, may also contribute enhanced freshening, the correlation between runoff and the summer atmospheric circulation is consistent with other studies evaluating individual links between the summer atmospheric forcing and glacial runoff (Hanna et al., 2013, 2021), and the resulting freshwater input into the North Atlantic (Bamber et al., 2018; Dukhovskoy et al., 2019).

With the majority of seasonal runoff arriving in the subpolar gyre during autumn (Fratantoni and McCartney, 2010; Schmidt and Send, 2007), the change in the surface salinity from summer (August) to winter (January to March) has previously been estimated by evaluating Eq. (1) for a shallow surface layer (Oltmanns et al., 2020). Thus, the summer NAO, multiplied by '−1' was identified as a suitable index for the seasonal freshwater that reaches the subpolar region between August and winter (Fig. 3b). The timing of the increased seasonal freshwater input associated with $-NAO_S$ supports the role of seasonal runoff and melting for the $F_E$ freshwater anomalies, since they are preceded by a strongly negative summer NAO.

While the full, un-subsampled summer NAO is a suitable indicator of the seasonal freshwater input from summer to winter, it is not necessarily correlated with absolute SSS anomalies in winter. Once a seasonal mixed layer is eroded, the SST and surface salinity are expected to be influenced by other factors, consistent with the nonlinear relationship between the summer NAO and subsequent winter SST anomalies (Fig. 1d).

Among the dominant drivers of deeper freshwater anomalies is the subpolar gyre circulation. Specifically, a stronger subpolar gyre circulation, particularly in the northwestern subpolar region, has been found to lead to enhanced inflow of fresh and cold polar water from the coastal Labrador Current into the subpolar gyre (Häkkinen and Rhines, 2009; Häkkinen et al., 2011a, 2013; Koul et al., 2020). Since the subpolar gyre circulation is, in turn, largely forced by the wind stress (Häkkinen et al., 2011b; Spall and Pickart, 2003), earlier studies have identified a significant link between a stronger wind stress curl over the subpolar North Atlantic and a reduced salinity in the subpolar gyre (Häkkinen and Rhines, 2009; Häkkinen et al., 2011a, 2013; Hátún et al., 2005; Holliday et al., 2020).

To assess the role of the wind stress curl and subpolar gyre circulation for the cold and fresh anomalies associated with higher summer NAO states, we inspect the associated absolute dynamic topography in winter. The full, un-subsampled summer NAO only displays a weak and mostly non-significant relationship with the geostrophic surface circulation in the southwest subpolar region (Fig. 3c). When using the sub-sampled summer NAO corresponding to the $F_W$ subset, however, the absolute dynamic topography north of 50 °N in winter is significantly reduced, implying a more cyclonic and hence, stronger subpolar gyre circulation in the northwest subpolar region (Fig. 3d). The strengthened relationship between the subsampled summer NAO and the subpolar gyre circulation thus supports the subsampling by providing a physical explanation for the freshwater anomalies associated with $F_W$ (Fig. 2b).
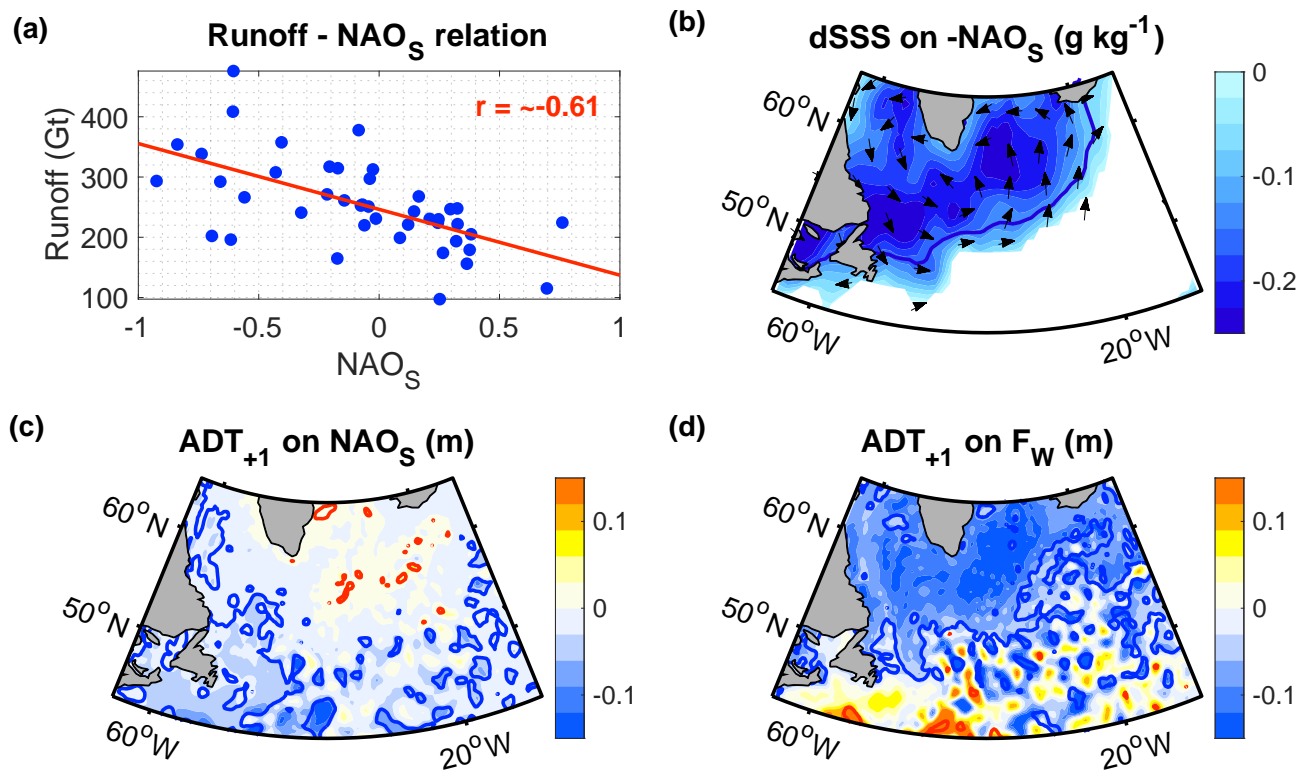
**Figure 3.** (a) Relationship between the NAO in July and August (NAO$_S$) and the runoff integrated over the Greenland ice sheet and over July and August. (b) Regression of the newly arriving, seasonal surface freshening between summer (August) and winter (January to March) onto $-$NAO$_S$ from the preceding summer. dSSS corresponds to the SSS change from summer and winter, estimated using a mass balance analysis (Oltmanns et al., 2020). The arrows represent the mean geostrophic surface flow, obtained from the absolute dynamic topography, averaged from August to March (the period of the freshening). Multiplying the summer NAO by '$-1$' serves the purpose of using an index that is positively correlated with the surface freshening. (c,d) Regression of the absolute dynamic topography in winter (January to March) onto (c) NAO$_S$ and (d) F$_W$ from the preceding summer. Contours encompass regions that are significant at the 95% confidence level.

While a detailed quantification of freshwater budget is beyond the scope of this study, the proposed physical causes of the obtained freshwater estimates are supported by their spatial characteristics and intensities. $F_W$ freshwater anomalies are largest over the western subpolar region, where the subpolar gyre circulation is strongest and where the surface heat fluxes are largest, and can erode seasonal freshwater anomalies more easily. $F_E$ freshwater anomalies are largest over the southeastern part of the subpolar region where surface fluxes and the subpolar gyre circulation are weaker, and where the mixed layer depths are shallower. We also examined the associated surface fluxes (precipitation minus evaporation) but found that they were too small to account for freshwater anomalies. In autumn and winter, moreover, the surface freshwater fluxes were evaluated as part of the buoyancy fluxes in the surface mass balance and found to be negligible.

## 4.3 Atmosphere-ocean circulation in winter

Next, we examine the large-scale atmosphere circulation associated with both types of freshwater anomalies. We focus on the anomalies that are represented by the $F_E$ subset (Fig. 2a) due to their sharper SST signals. However, freshwater anomalies associated with the $F_W$ subset show qualitatively similar atmospheric responses, both in winter (not shown) and in summer (Section 4.4).

Since the meridional SST gradient is increased in winters after stronger freshwater anomalies, there is a sharper SST front between the subtropical and the subpolar gyre, pariticularly over the western North Atlantic (Fig. 1e). Directly above this sharper SST front, we observe an amplified baroclinic instability in the atmosphere, indicated by an enhanced Eady growth rate (Fig. 4a).

The amplified baroclinic instability manifests itself in a distinct circulation anomaly. When an air parcel travels northward across the SST front, it rises because it is warmer than the surrounding air masses. By rising, the air column stretches, acquiring positive vorticity. The opposite occurs when an air parcel travels southward across the front. Consistent with the resulting enhanced baroclinic wave activity, the observations show a cyclonic anomaly north of the SST front and an anticyclonic anomaly to the south (Fig. 4b), representative of a positive NAO phase. Thus, the observed atmospheric circulation anomaly is consistent with the underlying SST pattern and the observation that, after strong $F_E$ anomalies, the NAO anomaly switches sign from being strongly negative in summer to being strongly positive in winter.

The obtained atmospheric circulation anomaly drives a convergent Ekman transport between the subtropical and subpolar gyre (Fig. 4b), leading to an increase in sea level. This Ekman transport is a direct response to the associated wind forcing but the resulting increase in sea level and horizontal pressure gradients can have longer lasting repercussions. Indeed, the increased sea level and associated ocean instabilities manifest themselves in a broad band of anti-cyclonic eddies that extends into the second winter after the freshwater anomalies (Fig. 4c). The eddies are not visible in the SST due to the coarser $1° \times 1°$ grid spacing of the SST product, compared to the $0.25° \times 0.25°$ grid spacing of the absolute dynamic topography product.

Considering that the mean flow along the eddies is eastward, representing the North Atlantic Current, the integrated effect of the anti-cyclonic eddies is a reduced eastward speed at the southern edge of the band and an increased eastward speed at the northern edge (Fig. 4d). This circulation pattern has been referred to as inter-gyre gyre circulation (Marshall et al., 2001) and is equivalent to a northward shift of the North Atlantic Current (Kostov et al., 2021; Zhao and Johns, 2014).
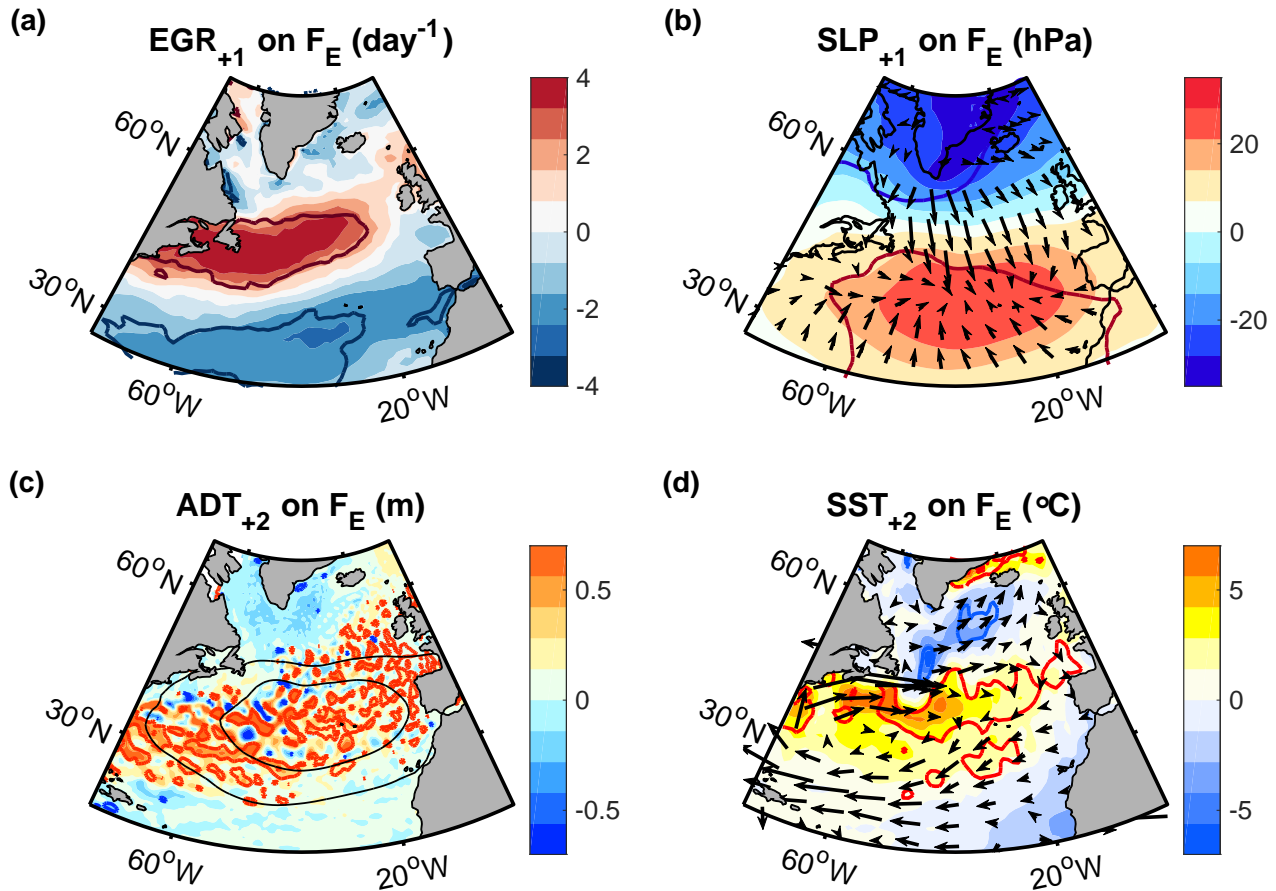
**Figure 4.** Regressions of (a) the maximum Eady growth rate, (b) the sea level pressure, (c) the absolute dynamic topography (ADT) and (d) the SST in winter (January through to March) on $F_E$. (a) and (b) are in the first winter after the anomalies whereas (c) and (d) are in the second winter after $F_E$ (indicated by the '+1' and '+2' in the title). The arrows in (b) show the direction of the associated Ekman transports. The arrows in (d) represent the smoothed geostrophic flow implied by the ADT anomaly. The thin black contours in (c) show the region of Ekman flow convergence from (b). Thick contours in all panels encompass regions that are significant at the 95% level.

The northward shift of the North Atlantic Current implies a large-scale warm SST anomaly to the south of the subpolar cold anomaly, not because the water inside the current is anomalously warm but because the current occurs at an anomalously northward location. This warm SST anomaly is seen in the first, and the second winter after freshwater anomalies (Fig. 1e and 4d). However, in the first winter, the northward shift is partially obscured by the wind-driven, southward expansion of the cold SST anomaly over the eastern North Atlantic, potentially driving enhanced mixing and erosion of the SST front. The spatial distribution of the surface heat fluxes, on the other hand, does not match the SST field (Fig. A1d), indicating that the contribution of the surface heat fluxes to the warm SST anomaly is limited. While this mechanism has been demonstrated using the $F_E$ subset, the signals for the $F_W$ subset are qualitatively the same but confined to only the first winter.

We summarise that freshwater anomalies are associated with cold anomalies in the subpolar region in winter (Fig. 1e and f). The cold anomalies form part of an enhanced meridional SST gradient, implying a sharper SST front between the subpolar gyre and the subtropical gyre. The sharper SST front is associated with an amplified baroclinic instability in the atmosphere (Fig. 4a) that is characterised by a more cyclonic circulation anomaly over the subpolar gyre and a more anticyclonic anomaly to the south (Fig. 4b). This atmospheric circulation anomaly sets up surface pressure gradients through Ekman transports, which drive a geostrophic flow that contributes to the warm anomaly south of the subpolar cold anomaly (Fig. 4c and d).

The overall effect of the ocean-atmosphere coupling is a sharper SST gradient between the subtropical warm anomaly and the subpolar cold anomaly, which is characteristic of the large-scale SST tripole pattern and associated feedbacks (Czaja and Frankignoul, 2002; Marshall et al., 2001). By being highly correlated with the SST anomalies, the freshwater indices serve as valuable tools for visualising the associated ocean and atmospheric circulations, reinforcing each other (Figs. 1 and 4). However, we do not causally attribute the SST pattern to freshwater anomalies, and we do not infer that the freshwater anomalies act as a trigger for the characteristic tripole SST pattern.

## 4.4 Links to European summer weather

The preceding analysis revealed a close statistical link between freshwater anomalies and associated winter conditions. Next, we investigate the SST and atmospheric conditions in subsequent summers. In the first summer after stronger freshwater anomalies (again represented by $F_E$), we find that the SST is characterised by an enhanced subpolar cold SST anomaly covering part of the North Atlantic Current in the central North Atlantic (Fig. 5a). In the second summer, the northward shift of the North Atlantic Current is the most pronounced signal, visible by a band of increased SST that extends northeastward across the North Atlantic from Nova Scotia towards the British coast (Fig. 5b).

The SST signal in both summers after the freshwater anomalies implies an increased SST difference between the warm subtropical gyre and the cold subpolar gyre. The exact location of the SST front between the subtropical gyre and the subpolar gyre can differ between the years included in the subset and is therefore poorly constrained, resulting in reduced significances at individual grid points. However, the increased SST gradient — which is of greater dynamical relevance than absolute SST anomalies — is highly significant. For instance, the SST difference between the region in which the SST anomaly exceeds 2 °C and the region in which the SST anomaly falls below −2 °C, includes a substantial area of the extra-tropical North Atlantic

(Fig. 5a and b) and is significantly correlated with the $F_E$ index with a correlation coefficient well above 0.7 in both summers (r ≈ 0.76 and 0.84 in the first and second summer respectively), with p-values well below 0.05.

As in the preceding winters, we find that the atmospheric circulation is aligned with the underlying SST in both the first and second summer after the freshwater anomalies, with the winds at 700 hPa circulating cyclonicly around the subpolar cold SST anomalies (Fig. 5a and b). In summer, however, there is an additional temperature contrast across the European coast. Thus, we observe a northward deflection of the jet stream downstream of the cold SST anomaly along the coast (Fig. 5c and d). In the first summer, the northward deflection occurs west off northern Africa, Spain, Portugal, France and the British coastline (Fig. 5c). In the second summer, the northward deflection of the jet stream occurs further north to the northwest of the Scandinavian coastline (Fig. 5d), consistent with the more northerly SST front over the North Atlantic (Fig. 5a and b).

In line with the more northerly SST front and jet stream locations in the second compared to the first summer, we observe relatively warmer and drier air over northern Africa and southwest Europe in the first summer after stronger freshwater anomalies, and relatively warmer and drier air over northwest Europe in the second summer (Fig. 5e-h). In the first summer the maximum warm anomalies extend from Morocco and Algeria northward to France and southern Germany, while the maximum dry anomalies occur further to the east covering large parts of southwest Europe, including Italy and Greece. In the second summer after the freshwater anomalies, the maximum warm anomalies occur over central to northern Europe, including Germany, France, the UK, Poland and southern Sweden, while the maximum dry anomalies again extend further eastward, including Finland and the Baltic countries. Considering that precipitation anomalies preferentially occur along trailing cold fronts and are shifted southward relative to cyclone centres (Booth et al., 2018; Kodama et al., 2019), the observed displacement of the dry anomalies relative to the warm anomalies is expected from their locations within individual weather systems and consistent with other studies (Yu et al., 2023).

Similar to the $F_E$ freshwater anomalies, freshwater anomalies associated with the $F_W$ subset are also followed by a cold SST anomaly in the subsequent summer. However, compared to $F_E$ freshwater anomalies, the cold SST anomalies associated with the $F_W$ index are smaller and confined to the central and western North Atlantic off the coast of Newfoundland, with the regressions peaking in July and August (Fig. 6a). Consequently, we observe a sharp northward deflection of the jet stream just eastward of the cold anomaly, and further west compared to the $F_E$ subset (Fig. 6b). Likewise, the warm air temperature anomalies over Europe also occur further west and are centred over France, Great Britain, Belgium and northern Spain, extending westward of the coast, while the dry anomalies extend eastward to the Baltic Sea region and northern Poland (Fig. 6c and d).

Overall, we find that the regressions of the SST and atmospheric circulation on $F_W$ are weaker compared to those on $F_E$, consistent with weaker freshwater anomalies (Fig. 2) and smaller regression slopes (Fig. 1d), implying weaker sensitivities to the freshwater index and associated atmospheric circulation in the preceding summer. Yet, despite differences in the location and magnitude of the anomalies, the overall patterns are qualitatively similar after $F_E$ and $F_W$ freshwater anomalies: Both types of freshwater anomalies are characterised by a cold SST anomaly and northward deflection of the jet stream over the North Atlantic in the subsequent summer. In both cases, the northward deflection of the jet stream reduces the advection of moist, maritime air masses over parts of Europe, resulting in warmer and drier weather over parts of Europe.
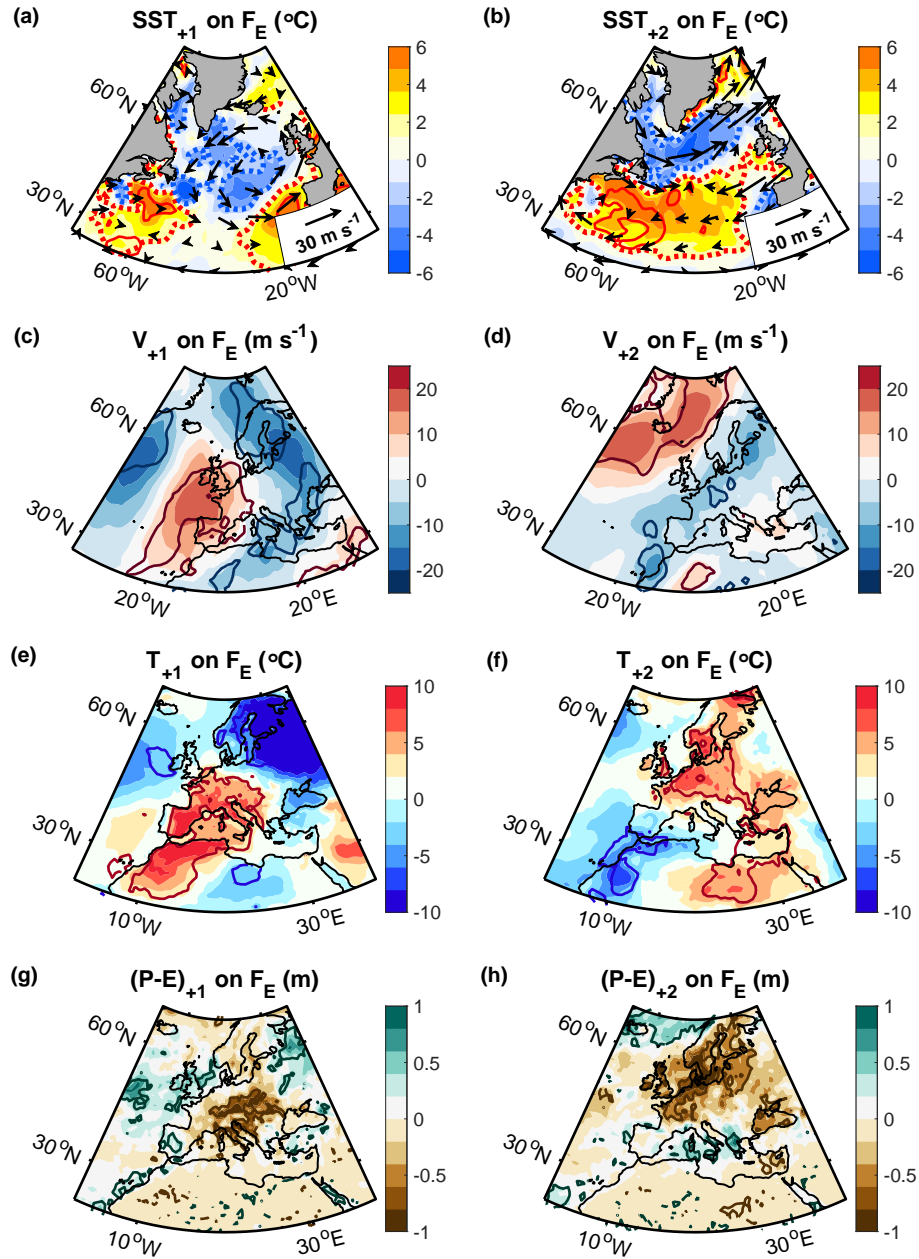
**Figure 5.** Regressions of (a,b) the SST (colour shading) and 700 hPa winds (arrows), (c,d) the meridional winds at 700 hPa, (e,f) the 2-m air temperature and (g,h) the accumulated precipitation minus evaporation on $F_E$ in (a,c,e,g) the first and (b,d,f,h) the second summer (May through August) after the freshwater anomalies (indicated by the '+1' and '+2' in the titles). We removed large-scale trends from the air temperature to reduce the direct warming effect of greenhouse gases (Section 2), and we excluded the anomaly in 2016 since its responses were covered by the 2017 anomaly (not shown). Thick contours encompass regions that are significant at the 95% confidence level and the red and blue dotted lines in panels a and b delineate the regions in which the the SST anomalies exceed 2 °C and fall below −2 °C.
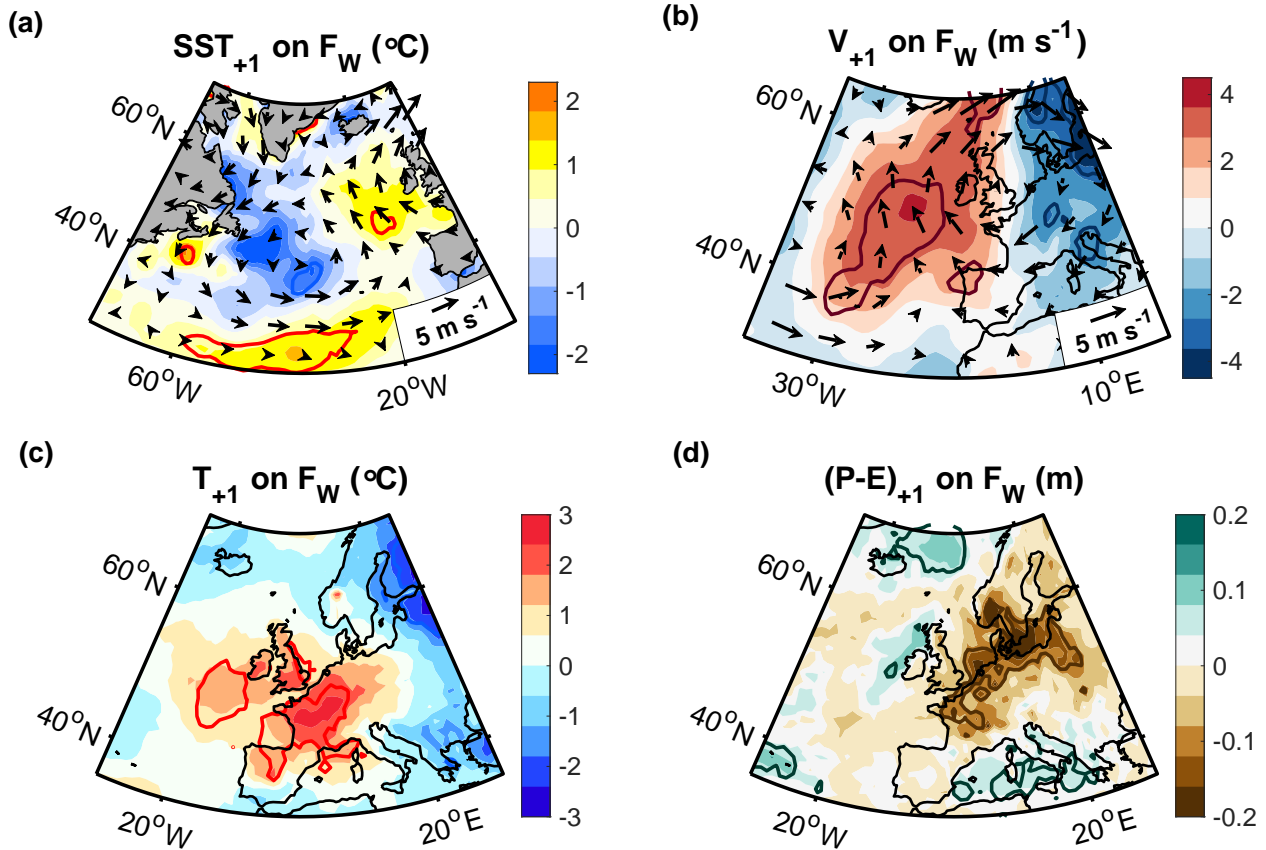
**Figure 6.** Regressions of (a) the SST (colour shading) and the 700-hPa winds (arrows), (b) the meridional winds at 700 hPa, (c) the 2-m air temperature and (d) the precipitation minus evaporation in summer (July and August) on $F_W$ from the preceding summer, again after subtracting large-scale trends from the air temperature. The thick contours encompass regions that are significant at the 95% confidence level.

## 4.5   Significance and robustness

The significance of the relationships between the freshwater indices and the ocean and atmospheric conditions in the subsequent winter and summer was assessed by Student t-tests, noting that the subsampling does not affect the significance of the relationship between the indices and any variable that is statistically independent of freshwater. If there is no connection to freshwater anomalies, the probability for randomly obtaining a significant statistical link by chance remains the same.

Thus, we obtained significant links above the 95% confidence level, indicating that the probability for randomly obtaining the identified links is less than 5%. To ensure that the results are robust, we repeated the regressions by changing the number of years included in the subsampling, and by excluding anomalies in consecutive years (Appendix B). In all cases, we find that the identified links are robust, which is consistent with the scatter diagram (Fig. 1d), showing that there are no outliers or clusters of values responsible for the high correlations.

A limitation of $F_E$ and $F_W$ is that they only cover a limited set of years, raising the question if the relationship between the SST, SSS and subsequent atmospheric anomalies holds generally or only over the selected subsets. To address this question, we use an un-subsampled SST-based index covering all years. As before, we avoid potential influences of a spatially uniform warming trend by using the spatial SST differences between the subpolar and the subtropical gyre ('$\Delta$SST'), rather than absolute cold anomalies. Specifically, we use the SST difference between regions enclosed by the 95% lines, obtained after regressing the SST on $F_E$ (Fig. 7a). Using the regions obtained from $F_W$ does not appreciably change the results, as the associated $\Delta$SST time series (obtained from $F_E$ and $F_W$) are highly correlated with each other (r $\approx 0.96$, p $\approx 10^{-23}$).

Evaluating the surface mass balance associated with the new $\Delta$SST index, we again find that none of the terms on the righthand side of Eq. (5) can account for the mass increase, implied by the associated cold, subpolar SST anomaly (Appendix A). Thus, we conclude the cold anomaly can only be explained by the simultaneous existence of a freshwater anomaly, allowing us to infer the variability and spatial distribution of surface freshwater with an overall uncertainty of $\sim$6% that results from assuming density compensation. The correlation of the estimated freshwater variability with the $\Delta$SST index extends over the full subpolar region, with maximum amplitudes of up to $\sim$0.8 occurring in the eastern subpolar gyre (Fig. 7b). This correlation is slightly smaller than those obtained for the other two freshwater indices but the index now includes 44 years.

Considering the significant link between the $\Delta$SST index and surface freshwater in the supolar region, we use it as a new freshwater index and examine the ocean and atmospheric conditions in the subsequent summer. Inspection of the SST shows that a stronger $\Delta$SST index in winter is associated with pronounced cold SST anomaly over the central subpolar region in the subsequent summer (Fig. 7c). The atmospheric circulation is aligned with the underlying SST field, with the winds at 700 hPa circulating cyclonicly around the cold, subpolar SST anomaly (Fig. 7c). To the east of the cold SST anomaly, the winds are deflected northward along the European coastline (Fig. 7d), leading to warm and dry atmospheric anomalies over Europe. The warm anomalies extend over Spain, Italy France, the Netherland and parts of Germany eastward to Austria, Hungary and Slovakia, while the dry anomalies occur further northeastward, covering France, the Netherlands, Denmark, and parts of northern Germany, Poland and Ukraine (Fig. 7e and f).

Unlike the summer NAO, the new, SST-based index has higher autocorrelations (Fig. 8a), which we attribute to enhanced low-frequency variability of the North Atlantic climate in winter. We still assume that interannual variability substantially contributes to the correlations, due to the high, interannual variability of European summer weather, reflected in low autocorrelations (Fig. 8b). Nonetheless, to assess the contribution of low-frequency variability to the obtained links, we lowpass filter European summer weather with a hanning filter, using a window size of 3 summers to approximate the higher autocorrelations of the $\Delta$SST index (Appendix B). After accounting for the reduced number of independent samples in the significance tests with $N^* = \frac{N\Delta t}{2T_e} - 2$, where $N$ here refers so the number of data points, $\Delta t$ is the time interval between them, and $T_e$ is the e-folding timescale of the autocorrelations (Leith, 1973), we still obtain statistically significant relationships but the amplitudes of the regressions are reduced (Fig. B8), indicating that high-frequency, interannual variability substantially contributed to the relationship obtained from the unfiltered timeseries (Fig. 7).

To further assess the timescales on which the identified relationship holds and is significant, we carry out a multi-taper coherence analysis. Specifically, we calculate the coherence between the $\Delta$SST index and the temperature and precipitation minus
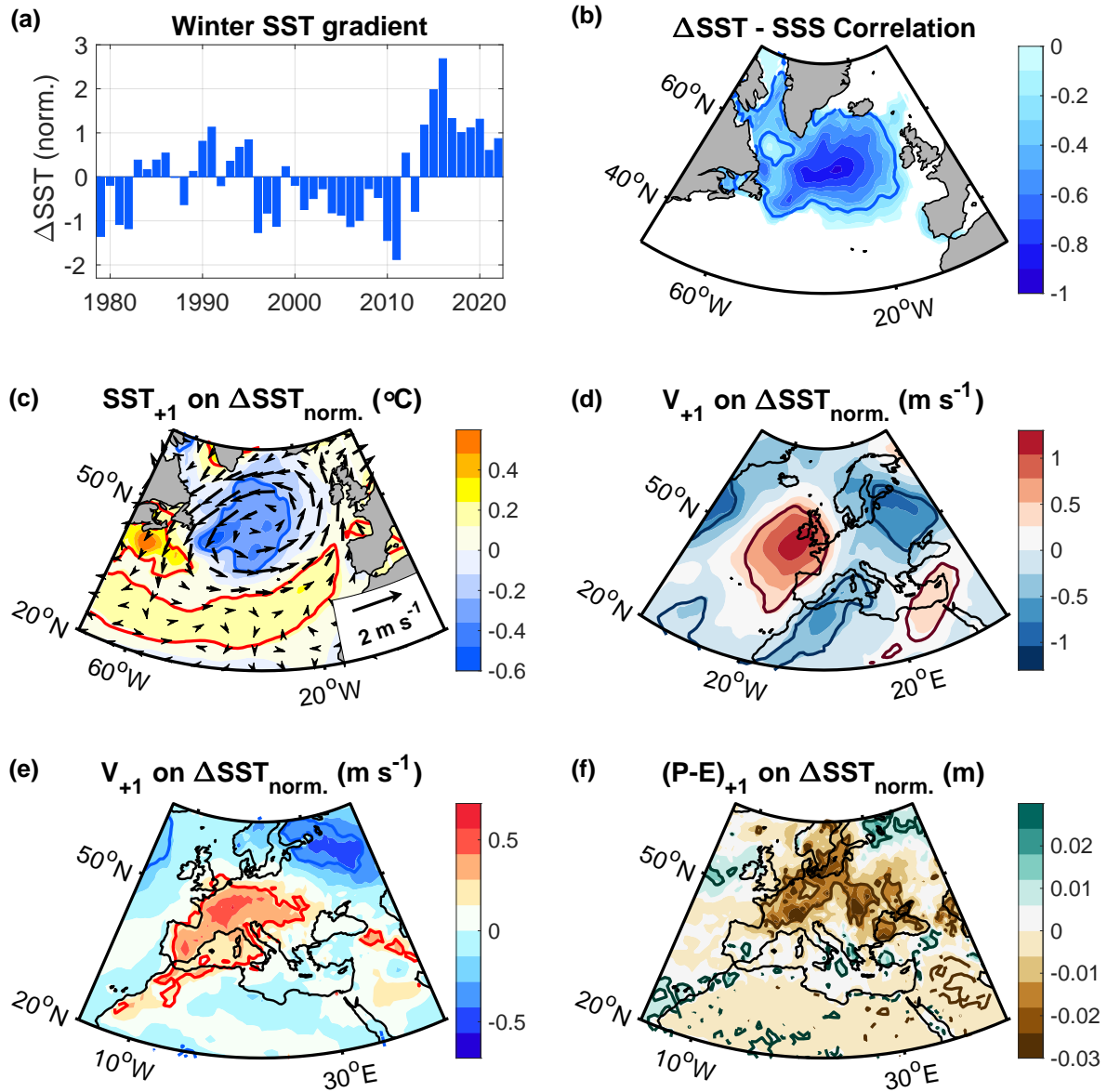
**Figure 7.** (a) ΔSST index corresponding to the normalised SST difference between the subtropical warm anomaly and the subpolar cold anomaly, enclosed within the 95% confidence lines in Figure 1e. (b) Correlation between the ΔSST index, shown in panel a, and the sea surface salinity anomaly in the same winter (January through March), estimated from the surface mass balance. (c-f) Regressions of (c) the SST (colour shading) and 700 hPa winds (arrows), (d) the meridional winds at 700 hPa, (e) the 2-m air temperature and (f) the precipitation minus evaporation in summer (July and August) onto the ΔSST index from the preceding winter (panel a), again after subtracting the large-scale trends from the air temperature. The thick contours encompass regions that are significant at the 95% confidence level.
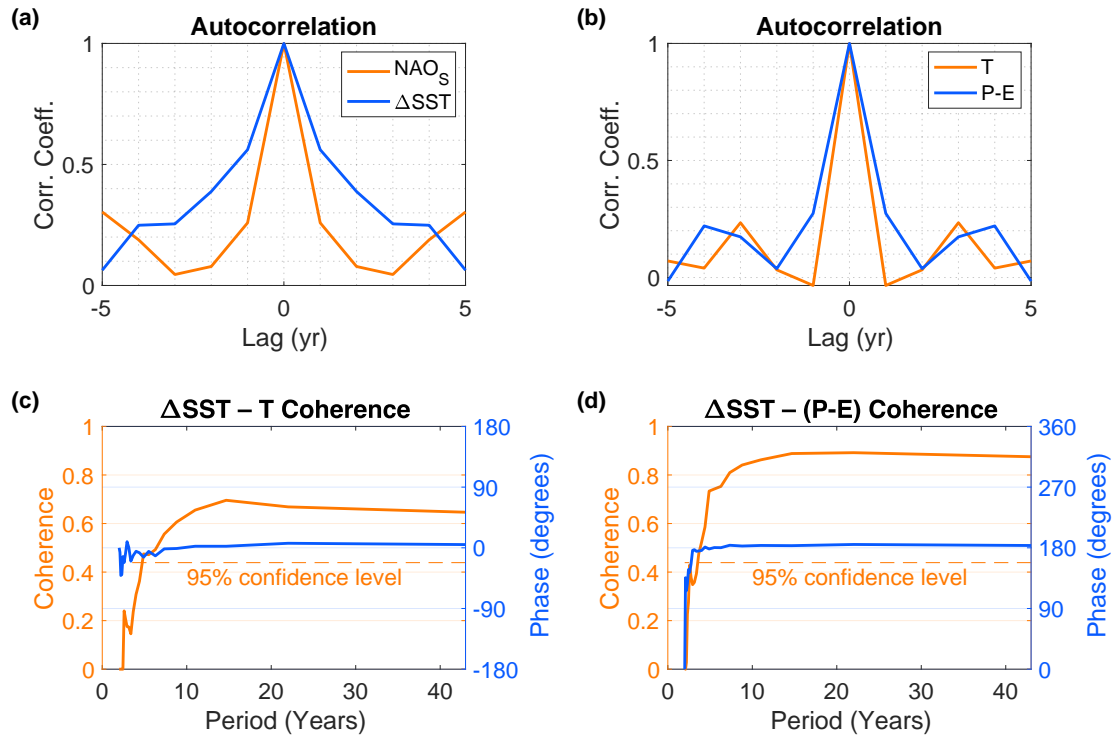
**Figure 8.** (a,b) Autocorrelations of (a) the NAO index in summer (July and August) and the $\Delta$SST index in winter (January to March), (b) the 2-m air temperature and precipitation minus evaporation anomalies in summer (July and August), averaged over the regions enclosed by the 95% confidence lines in Figure 7e and f. (c,d) Multi-taper coherence and phase shift estimates for the $\Delta$SST index in winter (January to March) and (c) the 2-m air temperature and (d) precipitation minus evaporation in the subsequent summer (July and August), again within the regions enclosed by the 95% confidence lines in Figure 7e and f. We used 8 tapers. The 95% confidence estimates are based on Amos and Koopmans (1963) after correcting for the bias inherent in coherence estimates (Priestley, 1982).

evaporation anomalies in the regions in which we identified a significant link from the regressions (Fig. 7e and f). Inspection of the coherence estimate shows that both, temperature and precipitation minus evaporation over Europe, are significantly linked to freshwater variations in the subpolar region on timescales from a few years to decades (Fig. 8c and d). The coherence between the $\Delta$SST index and the precipitation minus evaporation anomaly is particularly high and well above the 95% significance line (Fig. 8d). The associated phase shifts are relatively constant at 0° for the air temperature (indicating a positive correlation) and 180° for precipitation minus evaporation (implying anti-correlation). We used 8 tapers, which is a standard value. However, the results are not sensitive to this choice.

We conclude that the link between cold, fresh ocean anomalies in the subpolar North Atlantic region in winter and warm, dry atmospheric anomalies over Europe in the subsequent summer is robust, significant at both higher and lower frequencies, and independent of the spatial and temporal characteristics of the freshwater index that is used.

## 4.6 Predictability of European summer weather

The preceding analyses revealed significant links between North Atlantic freshwater anomalies and European summer weather in subsequent years. This raises the question to what extent this link can be used to predict European summer weather in advance. Thus, we next assess the predictability based on the explained variance in the observations, estimated by means of the squared correlation coefficient with the freshwater indices.

The variance of the near surface temperature and precipitation minus evaporation anomalies, explained by the $F_E$ subset, reaches and even exceeds 80% over large parts of Europe (Fig. 9a-d). For the $F_W$ subset, the explained variance drops to $\sim$50% (Fig. 9e and f), and for the $\Delta$SST index, the explained variance drops further to $\sim$20% (Fig. 9g and h), as expected from the trade-off between the number of years included in the index and the associated correlations with freshwater anomalies in the subpolar North Atlantic region in winter and European weather anomalies in the subsequent summer.

Overall, we find: The higher the correlation is between the initial freshwater anomaly and its index, the higher is also the variance of European summer weather that the index subsequently explains. The $F_E$ index, in particular, has an extremely high correlation with the initial freshwater anomaly of over $\sim$0.9 (Fig. 2c) and explains over 80% of the variance of European summer weather. Notwithstanding the small sample sizes — in the case of $F_E$ and $F_W$ — or the reduced correlations — in the case of the $\Delta$SST index — these results indicate that accurate estimates of the sea surface salinity in the subpolar region can serve as valuable constraints for predictions of European summer weather.

## 4.7 Warm summers in Europe

The preceding analyses showed that two types of freshwater anomalies with opposite atmospheric drivers (characterised by a high and a low NAO states in the preceding summer) are followed by cold anomalies over the North Atlantic in winter, shifts in the jet stream and warmer, drier weather over Europe in the subsequent summers. Lastly, we investigate if warm European summers can in turn be linked back to a freshwater anomaly in the preceding year. Thus, we assess the extent to which enhanced freshwater anomalies are not only a sufficient but also a necessary condition for warmer European summers.

Based on composites, we find that the 10 warmest relative to the 10 coldest summers in western Europe were associated with a dry anomaly to the east of the warm air temperature anomaly, a northward deflection of the jet stream west of Portugal, France and Britain, and a pronounced cold SST anomaly over the North Atlantic (Fig. 10a-e). Using a surface mass balance (Appendix A), we again trace the cold SST anomaly back to a freshwater anomaly in the preceding winter, with the freshwater anomaly covering a large part of the subpolar North Atlantic (Fig. 10f). Selecting different regions for the temperature variability over Europe shifts the location of the obtained jet stream and SST anomalies but does not qualitatively alter the results.

In conclusion, this composite analysis of Europe's warmest and coldest summers supports the statistical link between freshwater anomalies and European summer weather with an index based on air temperature. While the SST and NAO-based indices suggest that freshwater anomalies in the subpolar North Atlantic in winter are followed by warm and dry anomalies over Europe in the subsequent summer, the composite analysis additionally shows that the 10 warmest relative to the 10 coldest European summers have been preceded by significantly increased freshwater anomalies in winter.
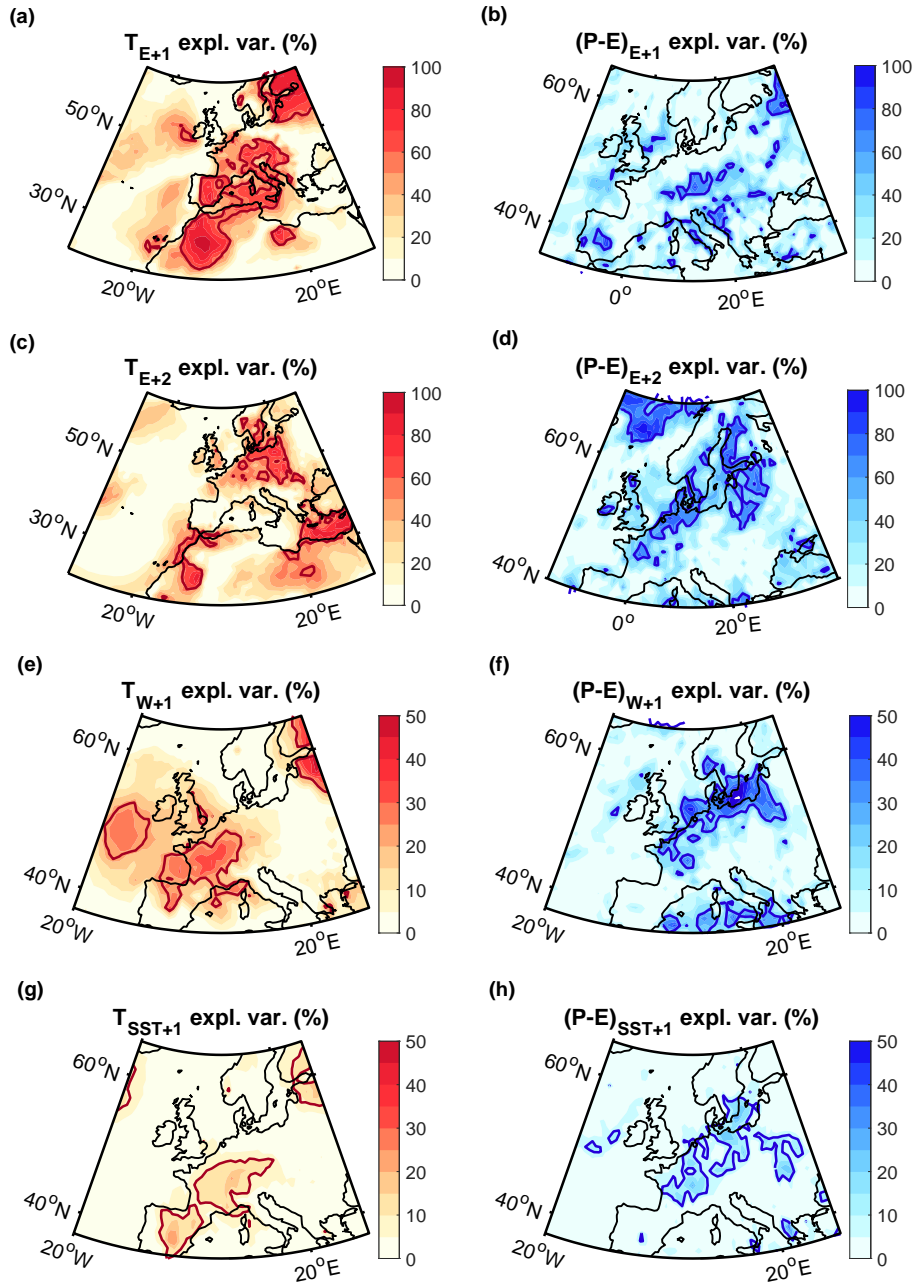
**Figure 9.** Variances explained by (a-d) $F_E$, (e,f) $F_W$ and (g,h) the $\Delta$SST index of (a,c,e,g) the 2-m air temperature and (b,d,f,h) precipitation minus evaporation after freshwater anomalies. '+1' and '+2' in the titles refer to the first and second summer after the freshwater anomaly. We again excluded the 2016 freshwater anomaly from $F_E$ since its responses were covered by the 2017 anomaly. Thick contours delineate the regions in which the correlation is significant at the 95% confidence level, assessed by means of two-sided Student t-tests. The explained variances were obtained from the squared correlation coefficients. Please note the different colour scales.
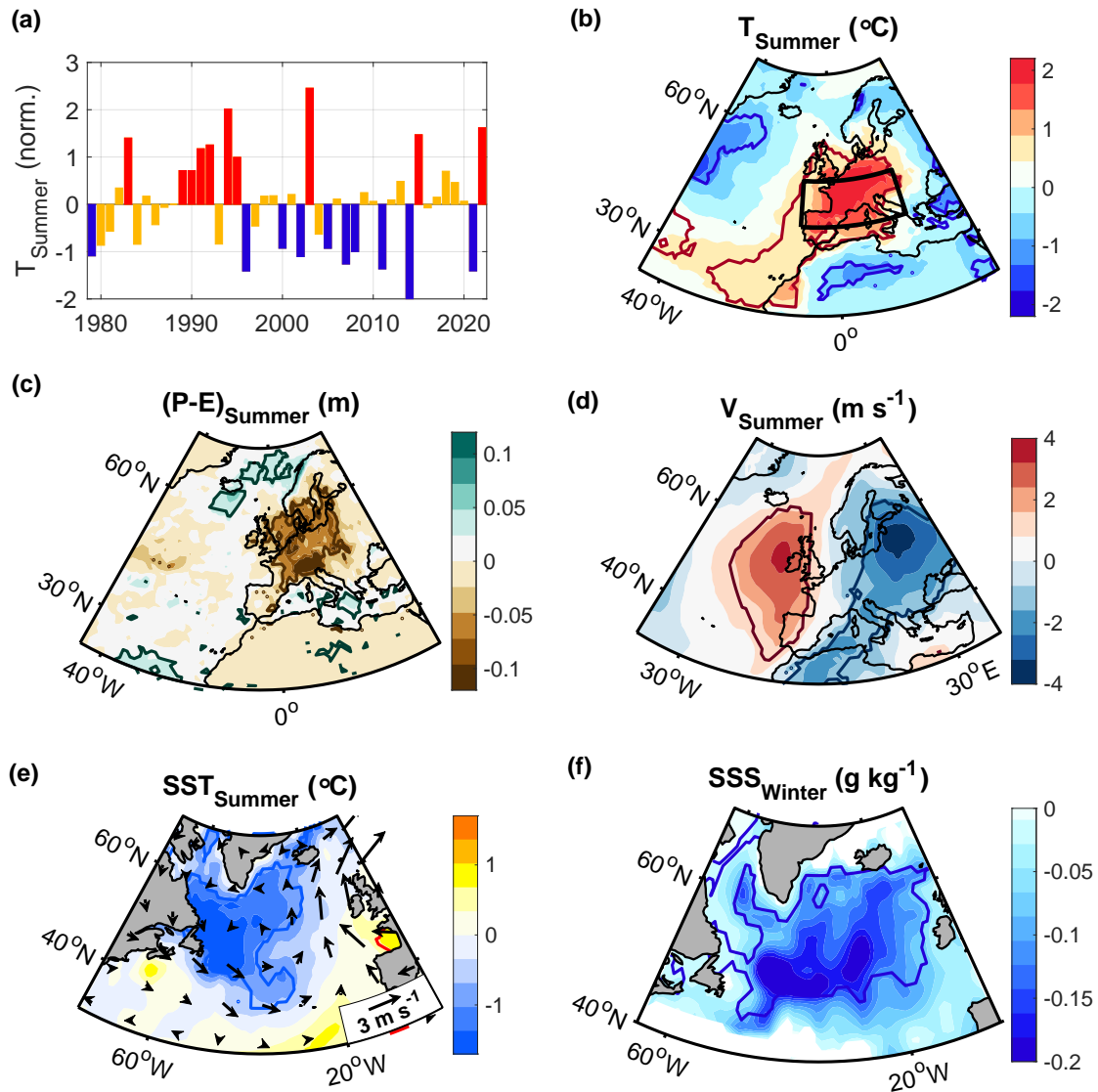
**Figure 10.** (a) Variability of the de-trended 2-m air temperature anomaly over land within the box shown in (b) during summer (July and August). (b,c,d,e) Composites of (b) the 2-m air temperature, (c) precipitation minus evaporation, (d) the meridional winds at 700 hPa, and (e) the SST (colour shading) and the 700 hPa winds (arrows) for the 10 warmest minus the 10 coldest summers, shown in (a). (f) Same as in (b-e) but for the sea surface salinity anomaly in the preceding winter, obtained from a surface mass balance (Appendix A). Contours delineate the regions that are significant at the 95% confidence level, assessed by means of two-sample t-tests.

## 5 Conclusions

In this study, we examined the link between North Atlantic freshwater anomalies and European weather in subsequent summers. Given the limitations of currently available salinity observations, we estimated the variability of freshwater based on a surface mass balance analysis. To identify statistical connections between the obtained freshwater estimates and European summer weather, we further applied regression and correlation analyses, composite analyses and multi-tapered coherence analyses. Combined, these analyses reveal a statistically significant relationship between freshwater anomalies in winter and European weather in the subsequent summer.

To understand the physical link between the identified, statistical connections, we examined the associated ocean and atmosphere circulations. Thus we found that enhanced freshwater anomalies are associated with subpolar cold SST anomalies and an increased SST front between the warm subtropical and the cold subpolar gyre in winter. The increased meridional SST gradient is linked to an amplified atmospheric instability and a large-scale atmospheric circulation anomaly with a more cyclonic circulation over the subpolar region and an anticyclonic anomaly to the south. This atmospheric circulation anomaly induces a northward shift in the North Atlantic Current which contributes to a warm anomaly to the south of the subpolar cold anomaly, amplifying the meridional SST gradient. In subsequent summers, the jet stream is deflected northward over the North Atlantic, aligned with the underlying SST fronts, leading to warmer and drier weather over Europe.

The obtained evolution of freshwater anomalies follows the chain of events expected from theory, indicating a coherent, deterministic mechanism that links North Atlantic freshwater anomalies to European summer weather. Yet, further studies are required to quantify the relative contributions of different ocean and atmospheric drivers and their uncertainties, and the role of freshwater as potential trigger of the identified chain of events. This study identified statistically significant links and thus indicates an enhanced predictability of European summer weather arising from freshwater anomalies in the North Atlantic, without attributing the variability of European summer weather to freshwater anomalies as a mechanical trigger.

Current numerical weather prediction systems show very limited to no forecast skill for European summer weather (Arribas et al., 2011; Dunstone et al., 2018). Thus, the existence of a link between North Atlantic freshwater anomalies and European summer weather indicates new potential to enhance the predictability of European summer weather a year in advance. Further studies that improve the representation of North Atlantic freshwater variations in models, and that quantify the predictability arising from them, are therefore desirable. In addition, targeted observational networks that monitor the variability of freshwater anomalies may help improve current forecast systems.

The melting of ice and runoff are expected to further increase in the coming decades (Notz and Stroeve, 2018; Briner et al., 2020), resulting in an enhanced freshwater discharge into the North Atlantic. With stronger freshwater anomalies, our results indicate an increase in the risk of warm, dry European summers and of heat waves and droughts accordingly. Unfortunately, global climate models have difficulties in capturing the hydrographic structure in the subpolar North Atlantic, including the distribution of freshwater (Menary et al., 2015; Heuzé, 2017; Liu et al., 2017; Sgubin et al., 2017; Mecking et al., 2017; Wu et al., 2018). Considering the identified links between freshwater anomalies and the subsequent ocean-atmosphere circulation, our results suggest that models may miss a key source of climate variability and potential long-range predictability.

*Code and data availability.* This study is only based on publicly available data and standard analysis techniques. The SST and NAO data are available from NOAA (https://psl.noaa.gov/data/gridded/data.noaa.oisst.v2.html and https://www.cpc.ncep.noaa.gov/products/precip/CWlink/

580   pna/nao.shtml). The Hadley SST data is available from https://www.metoffice.gov.uk/hadobs/hadisst/ and a complete merged NOAA and Hadley SST product can be obtained from https://gdex.ucar.edu/dataset/158_asphilli.html. Absolute dynamic topography data is distributed by the Copernicus Marine Environment Monitoring Service (https://marine.copernicus.eu/). ERA5 data can be obtained from the European Centre for Medium-Range Weather Forecasts (https://www.ecmwf.int/en/forecasts/datasets/reanalysis-datasets/era5) and the ECHAM5 and CAM5 model output can be downloaded from the Facility of Climate Assessments repository (https://psl.noaa.gov/repository/facts). Matlab

585   codes can be obtained from the corresponding author.

## Appendix A: Mass balance analyses

The following sections include the evaluation of the mass balances obtained from the freshwater indices $F_E$, $F_W$ and $\Delta$SST (A1), the surface mass balance obtained from the SST composite (A2), and a demonstration of the mass balance with hydrographic observations (A3).

### A1 Surface mass balance for freshwater indices

Taking advantage of the strong relationships between the $NAO_S$ subsets ($F_E$ and $F_W$) and the subsequent SST anomalies, we regress each term of Eq. (5) onto the indices and evaluate the surface mass balance over the subpolar cold anomaly regions within the 95% confidence lines (Figs. A1a and A2a).

Considering that mean mixed layer deepens from summer to winter, reaching its maximum in late winter, the integrated anomalies in the surface heat and buoyancy fluxes during autumn are predominantly driven by existing anomalies in the density profile. For instance, an anomalously warm and light layer of water will lead to increased ocean heat and buoyancy losses once it has been entrained (Timlin et al., 2002). Thus, given that the anomalies in $B_n$ and $M_n$ are expected to largely compensate for each other when integrated over autumn (the period of rapid mixed layer deepening), we focussed on the winter period (January through to March), when the amplitude and variability of the surface fluxes is largest. However, if we integrate the terms on the righthand side of Eq. (5) over autumn and winter, instead of only winter, the magnitude of the integrated anomalies does not appreciably change and their signs remain the same.

First, we estimate the convergence of mass ($A$). On the timescales and spatial scales considered, the strongest horizontal velocities result from the geostrophic surface flow (including eddies and the subpolar gyre circulation). These surface flows do not contribute to a net mass increase as they occur along lines of constant density and pressure. The largest ageostrophic surface flow in the open ocean results from the wind forcing, which we evaluate using the wind stresses from the atmospheric reanalysis ERA5. Integrated over the winter period (January through to March), we find that neither the horizontal Ekman transports nor the vertical Ekman pumping can account for the density increase associated with the cold anomaly. They are not significantly correlated with the freshwater indices, their amplitudes are too small, and their directions are inconsistent with the cold anomaly (Figs. A1a, b and A2a, b).

Next, we estimate the buoyancy flux anomalies $B = \frac{g\alpha}{c_p}Q + g\beta S(P - E)$, where $c_p$ is the heat capacity, $Q$ is the heat flux (positive downward) and $P - E$ is the freshwater flux in kg m$^{-2}$ s$^{-1}$ (Gill, 2016). After evaluating the buoyancy fluxes with 6-hourly ERA5 output and regressing them on the freshwater indices, we find that they do not match the distribution of the SST (Figs. A1c and A2c). The surface heat fluxes, which have the largest contribution to the buoyancy fluxes, are also not significantly correlated with the indices (Figs. A1d and A2d). When averaged over the cold anomaly regions, enclosed by the 95% confidence lines, and integrated over the winter, the buoyancy flux anomaly associated with the $F_E$ subset reflects an anomalous mass decrease of $\sim$7 kg m$^{-2}$ whereas the cold anomaly implies a mass increase of $\sim$204 kg m$^{-2}$. Likewise, the buoyancy flux anomaly associated with the $F_W$ subset reflects a mass decrease of $\sim$4 kg m$^{-2}$, whereas the cold anomaly implies a mass increase of $\sim$69 kg m$^{-2}$, using a mean density of $\rho_{mean} \approx 1000$ kg m$^{-3}$.
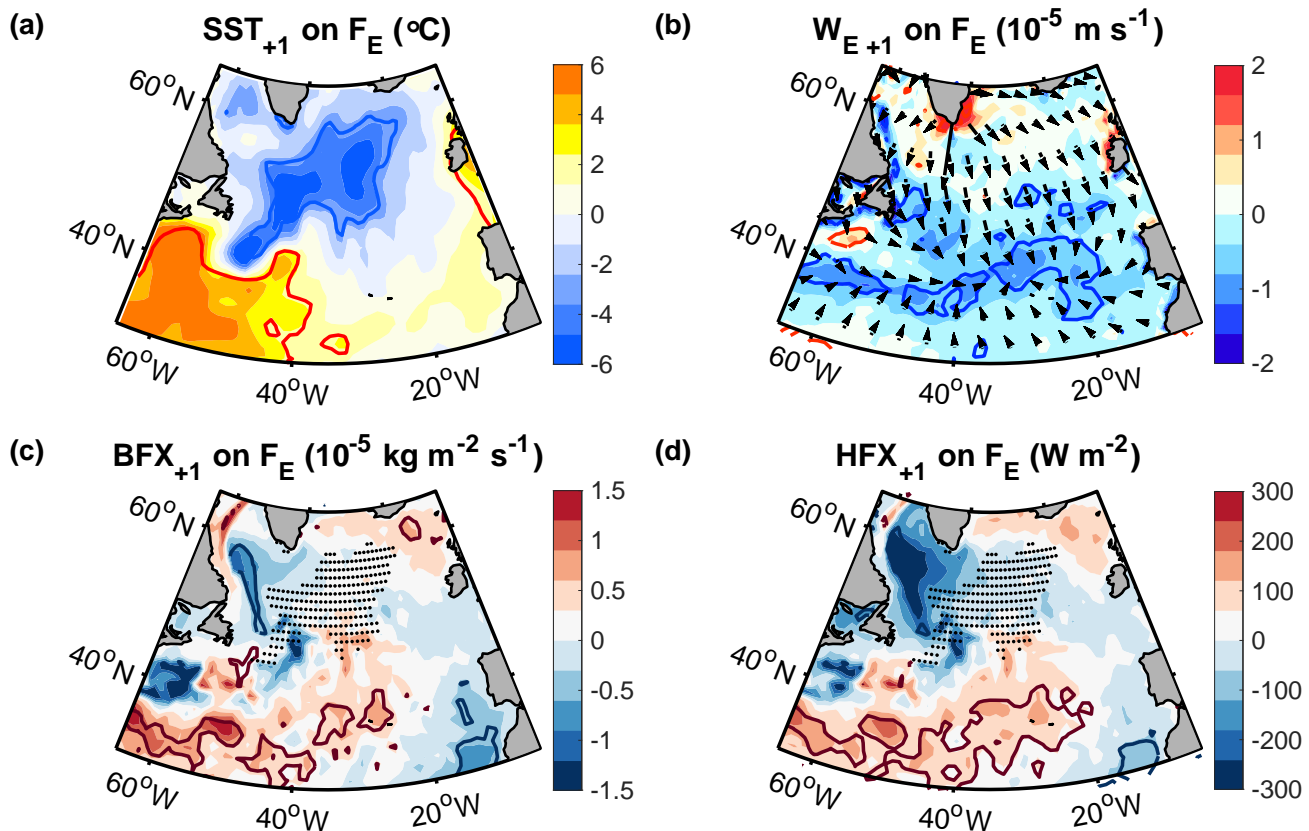
**Figure A1.** Regression of (a) the SST, (b) the vertical Ekman velocity (positive upward), (c) the buoyancy flux anomaly (positive downward) and (d) the surface heat fluxes (also positive downward) in winter (January through March) on $F_E$ from the preceding summer. The arrows in (b) indicate the direction of the horizontal Ekman transports and the dots in (c) and (d) show the region used for the mass balance calculations, corresponding to the cold anomaly region. Contours encompass regions that are significant at the 95% confidence level.

Since none of the potential, active drivers of density anomalies on the righthand side of Eq. (5) can account for the density increase associated with the cold anomalies, we conclude that the density increase associated with the cold anomalies must be balanced by a density decrease associated with freshwater anomalies. The buoyancy fluxes represent the largest term on the righthand side of Eq. (5), and thus determine the uncertainty of the obtained salinity estimates, amounting to ∼4% for the $F_E$ subset and ∼6% for the $F_W$ subset.

To verify the robustness of the results, we tested different integration periods and regions for the mass balance calculations. For instance, we also integrated the transports and surface fluxes from September to March instead of January to March, and we extended the investigated region over the full cold anomaly region, over which the SST anomaly is negative. In each case, the results did not change appreciably.
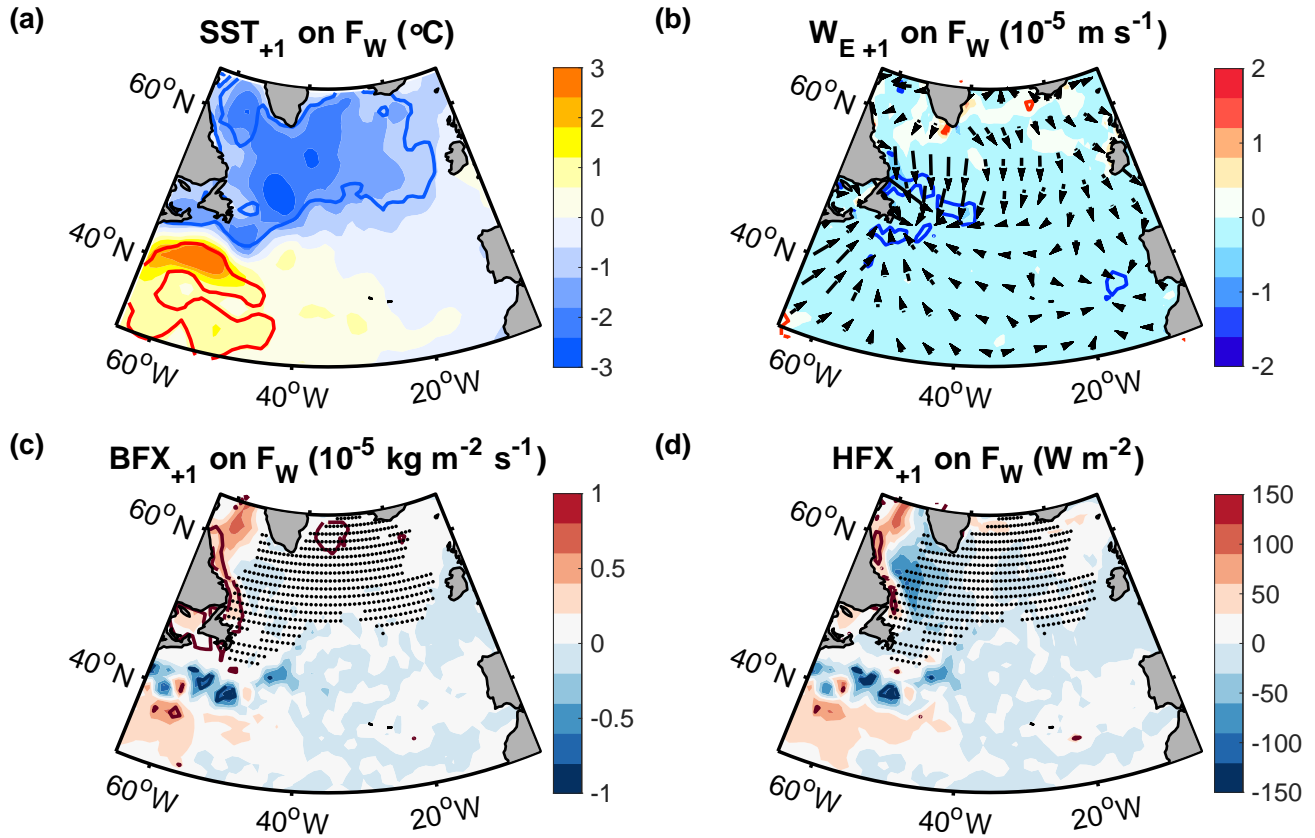
**Figure A2.** Regression of (a) the SST, (b) the vertical Ekman velocity (positive upward), (c) the buoyancy flux anomaly (positive downward) and (d) the surface heat fluxes (also positive downward) in winter (January through March) on $F_W$ from the preceding summer. The arrows in (b) indicate the direction of the horizontal Ekman transports and the dots in (c) and (d) show the region used for the mass balance calculations. Contours encompass regions that are significant at the 95% confidence level.

In addition, we repeated the analyses for the un-subsampled $\Delta$SST index (Fig. A3). In this case, we obtain a mean mixed layer depth of $\sim$250 m, a negative mass anomaly of $\sim -1$ kg m$^{-2}$ resulting from the surface buoyancy fluxes and a positive mass anomaly of $\sim +18$ kg m$^{-2}$ associated with the cold SST anomaly. Thus, estimating the sea surface salinity anomaly by assuming density compensation, we obtain a sea surface salinity of $\sim -0.10$ g kg$^{-1}$, averaged over the cold anomaly region enclosed by the 95% confidence lines with an overall uncertainty of 6% that results from neglecting the terms on the righthand side of Eq. (5).
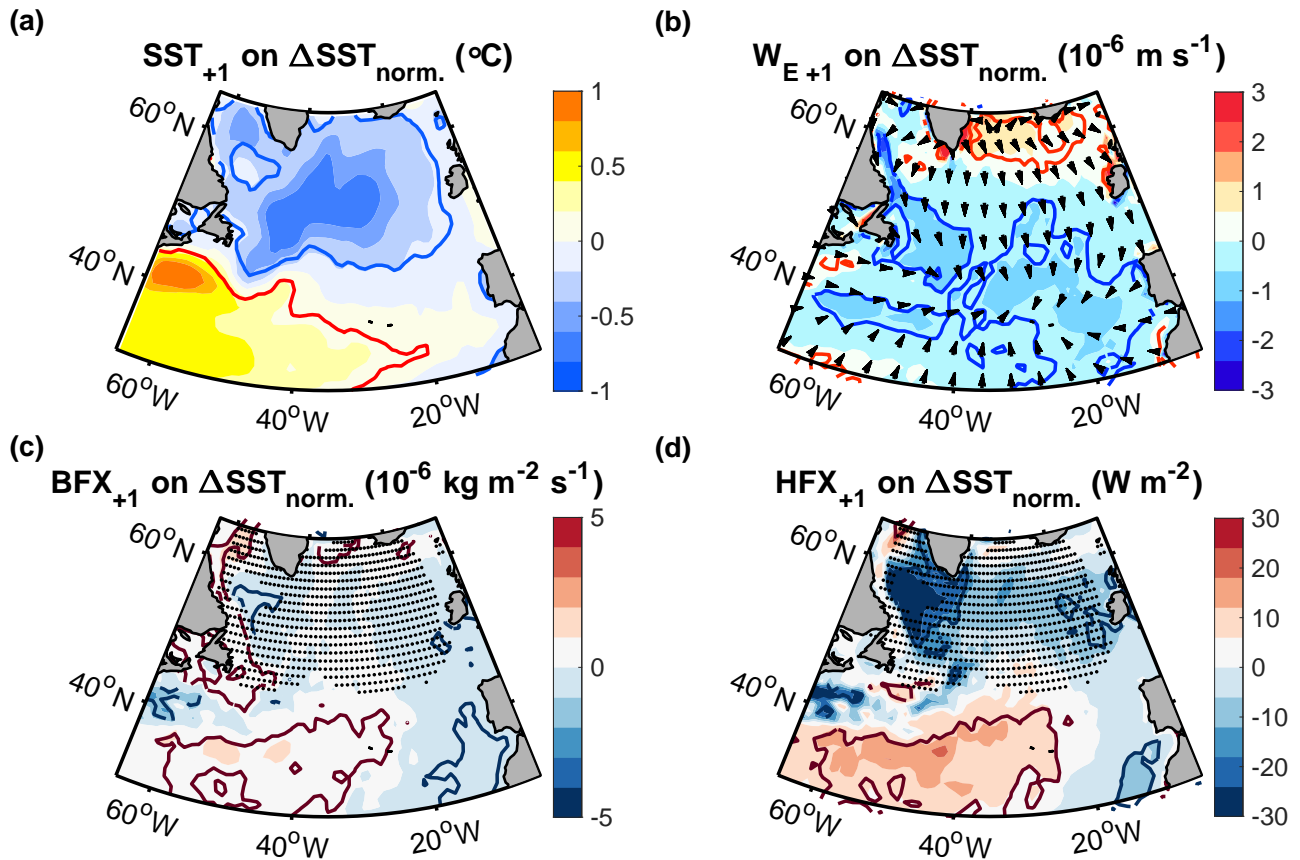
**Figure A3.** Regression of (a) the SST, (b) the vertical Ekman velocity (positive upward), (c) the buoyancy flux anomaly (positive downward) and (d) the surface heat fluxes (also positive downward) in winter (January through March) on the normalised $\Delta SST$ index (Fig. 7a). The arrows in (b) indicate the direction of the horizontal Ekman transports and the dots in (c) and (d) show the region used for the mass balance calculations. Contours encompass regions that are significant at the 95% confidence level.

## A2   Surface mass balance of the SST composite and trend

635   We further carried out a mass balance analysis for the composites of the cold anomaly in the winters preceding the 10 warmest relative to the 10 coldest summers over Europe (Fig. 10). Thus, we again evaluated the terms in Eq. (5) over the cold anomaly region and the winter, where now, the subscript $n$ refers to anomalies associated with the composites.

After evaluating each term in the mass balance equation, we obtain similar patterns compared to those associated with the two NAO subsets (Fig. A4). Again, we find that none of the density drivers on the righthand side of Eq. (5) show a significant

640   signal over the cold anomaly region, and their amplitudes cannot account for the density increase implied by the cold anomaly. The mean mixed layer depth in the cold anomaly region is now ~290 m, the surface buoyancy flux, which is the largest term

on the righthand side of Eq. (5), amounts to $\sim +1.2$ g kg$^{-1}$ while the density anomaly implied by the cold anomaly is $\sim -44$ g kg$^{-1}$. Thus, the uncertainty of the estimated freshwater anomaly (Fig. 10e) amounts to $\sim$3%.
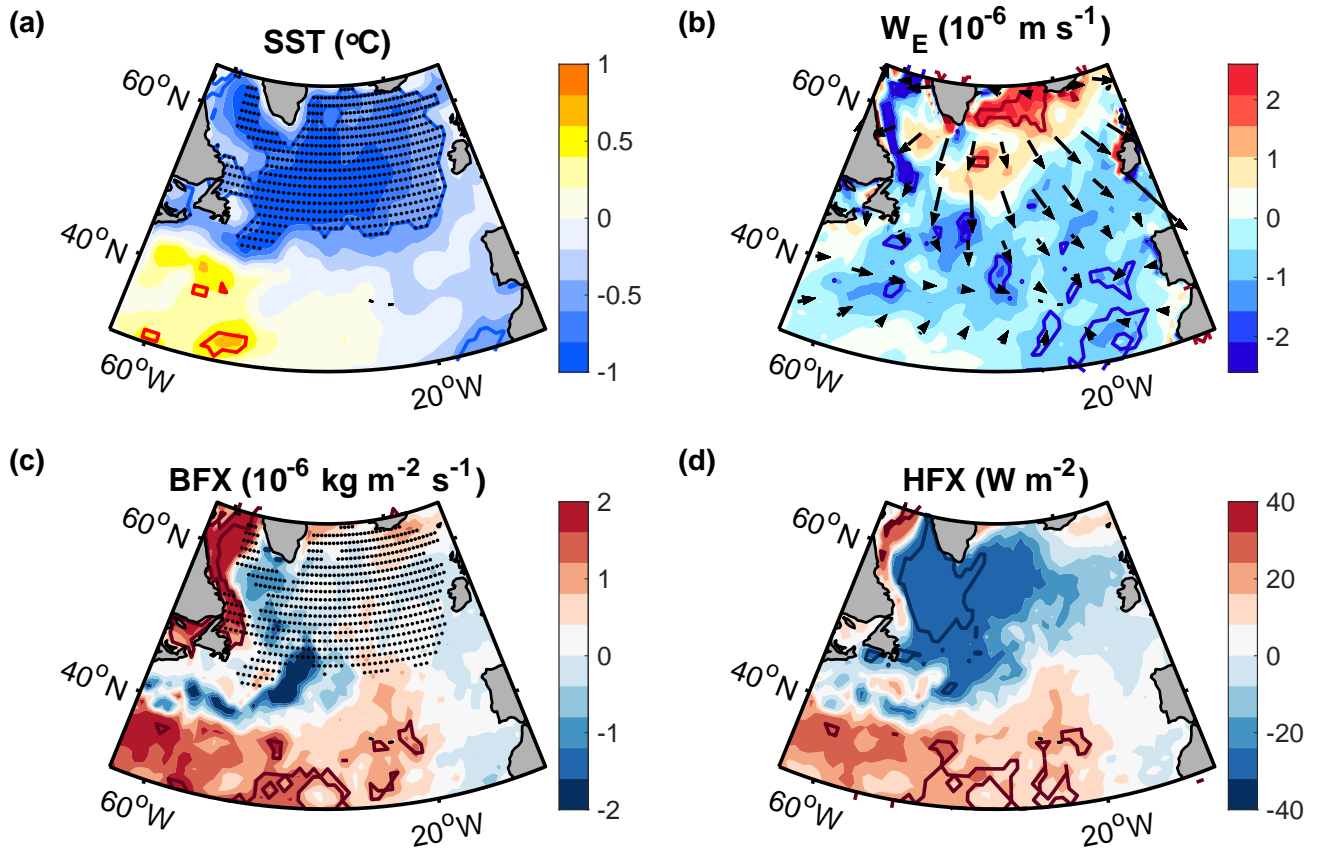
**Figure A4.** (a,b,c) Anomaly of (a) the SST, (b) the vertical Ekman velocity (positive upward), (c) the buoyancy flux anomaly (positive downward), and (d) the surface heat flux (also positive downward) in the 10 winters (January through March) before the warmest summers minus the 10 winters before the 10 coldest summers (Fig. 10). The arrows in (b) indicate the direction of the horizontal Ekman transports and the dots in (a) and (c) mark the region of the mass balance calculations.

### A3 Comparison with in-situ observations

645   To demonstrate the density compensation between temperature and salinity anomalies, we use mixed layer profiles from Argo floats in the subpolar region (Holte et al., 2017). We focus on the extreme winters 2015 and 2016, which were characterised by particularly large surface fluxes and deep convection (Yashayaev and Loder, 2017; Piron et al., 2017).

In both winters, the temperature and salinity anomalies are well-correlated with each other ($r \approx 0.72$, $p \approx 5 \cdot 10^{-242}$, based on 1532 profiles). Moreover, the observed salinity anomalies are well-aligned with the estimated salinity anomalies, obtained

650 by assuming density compensation (Fig. A5). The root mean square error associated with the mass balance estimate amounts to ∼0.09 g kg$^{-1}$, which is smaller than that of currently available salinity products (Bao et al., 2019; Xie et al., 2019).
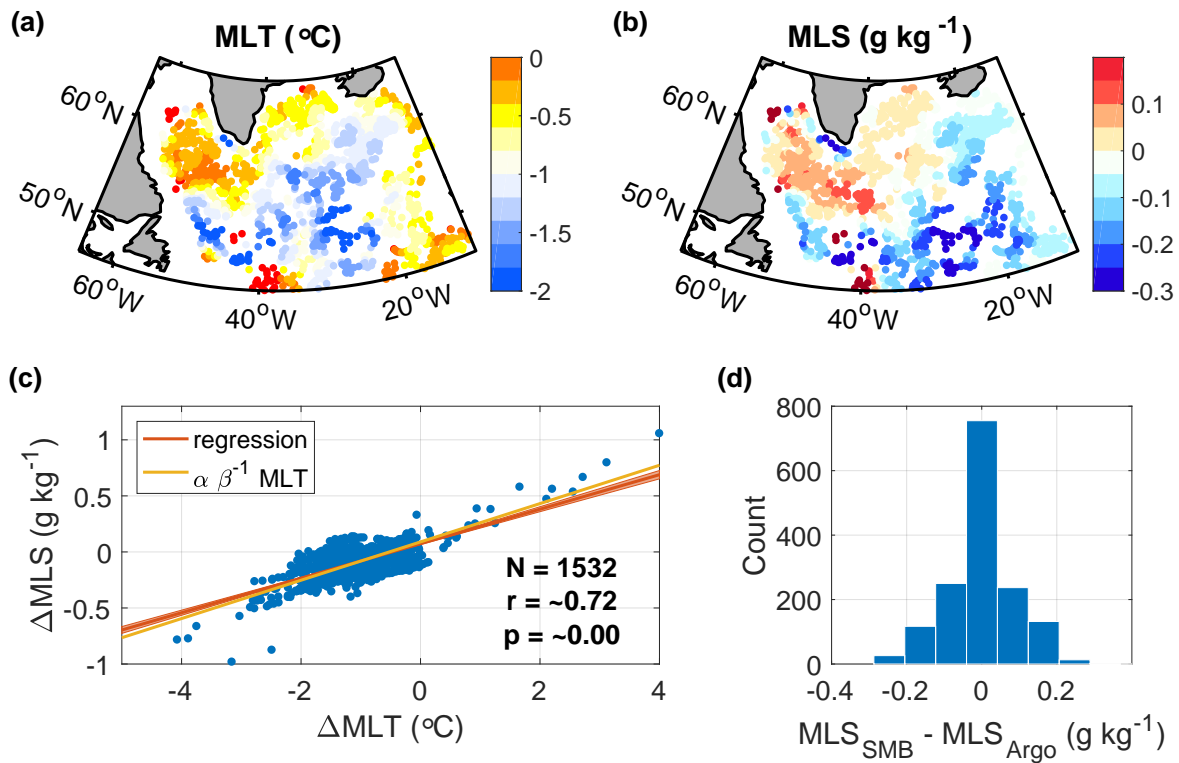
**Figure A5.** (a,b) Mixed layer temperature (MLT) and salinity (MLS) anomalies in the winters of 2015 and 2016 (January to April), derived from Argo profiles (Holte et al., 2017). The anomalies are relative to the climatological mean, estimated by averaging all other wintertime profiles within 2° longitude and 1° latitude. (c) Linear regression of the observed MLS anomalies on the MLT anomalies (red line), and the MLS estimate obtained by assuming density compensation (yellow line). (d) Differences between the estimated and observed MLS anomalies. The associated root mean square error is ∼0.09 g kg$^{-1}$.

## Appendix B: Robustness and significance tests

In this section, we conduct sensitivity tests to assess the robustness of the indices $F_E$, $F_W$, and $\Delta$SST. Considering the different weaknesses of each index, the analyses for each index are different. $F_E$ only includes a low number of years. Thus, we will test the sensitivity of the results to including and excluding individual years. For $F_W$, the sample size is larger, such that adding or removing individual years has almost no effect on the results. Thus, we will test the sensitivity of the results to the number of years included in increments of 5 years. Finally, the $\Delta$SSS index is characterised by high autocorrelations. Thus, we will test if the results remain significant if we lowpass filter European summer weather and assume a lower number of degrees of freedom.

We start with the $F_E$ subset. If we include the outlier in 2019 (which was removed as part of the subsampling in Section 3), we still obtain similar ocean and atmospheric conditions in the subsequent summers, compared to those with the outlier excluded (Figure B1 and Figure 5). Specifically, we still identify an increased SST difference between the subpolar cold SST anomaly and the subtropical warm SST anomaly, with the location of the SST front being shifted northward in the second summer relative to the first summer (Fig. B1a and b). Moreover, we still identify northward deflections of the jet stream and warm and dry anomalies over Europe (Fig. B1c to h), with the locations closely resembling the regressions with the NAO$_S$ year in 2019 excluded (Fig. 5c to h). Likewise, if we only include the second anomaly in all consecutive anomalies, the results also remain similar and significant (Fig. B2).

Next we examine the sensitivity of the results to the number of years included in the $F_W$ subset. Since we find that the results do not change appreciably when we include or exclude single years, we show how the results are changing when we add or remove years in increments of 5 years. Thus, we show the regressions for $N = 7$ (Fig. B3), $N = 12$ (Fig. B4), $N = 17$ (Fig. 6), $N = 22$ (Fig. B5), $N = 27$ (Fig. B6) and $N = 32$ (Fig. B7), with $N$ corresponding to the number of years included. The choice of years follows the same method as before (Section 3), with the objective of maximising the regression slope and the variance (resulting in high correlations). Thus, we rank all years according to the term $(y_i - y) \cdot (x_i - x_0)$ (Section 3.2) and then select the $N$ highest terms.

The regression for the case, where no further subsampling is applied after excluding the $F_E$ subset and the two outliers (corresponding to $N = 33$, not shown), do not change appreciably compared to the regression where $N = 32$. Likewise, if we exclude the only remaining consecutive year from the case where $N = 7$ (not shown), the results do not change appreciably compared to the $N = 7$ case. Overall, we find: The lower the number of years, the higher is the amplitude of the correlations and regressions, which compensate for the reduced number of degrees of freedom in the significance estimates. In addition to the higher amplitudes, the location of the maximum warm and dry anomalies can shift in accordance of the location of the associated summer SST anomalies. However, in all cases we identify an increased SST difference between the subpolar cold anomaly and the warm North Atlantic Current, a northward deflection of the jet stream west of the European coastline, and warm and dry atmospheric anomalies over parts of western Europe or the eastern North Atlantic.

Lastly, we tested if the results obtained with the $\Delta$SST index (Fig. 7) remain significant if we lowpass filter the atmospheric anomalies in summer and assume a smaller number of degrees of freedom. In the lowpass filtering, we only consider the
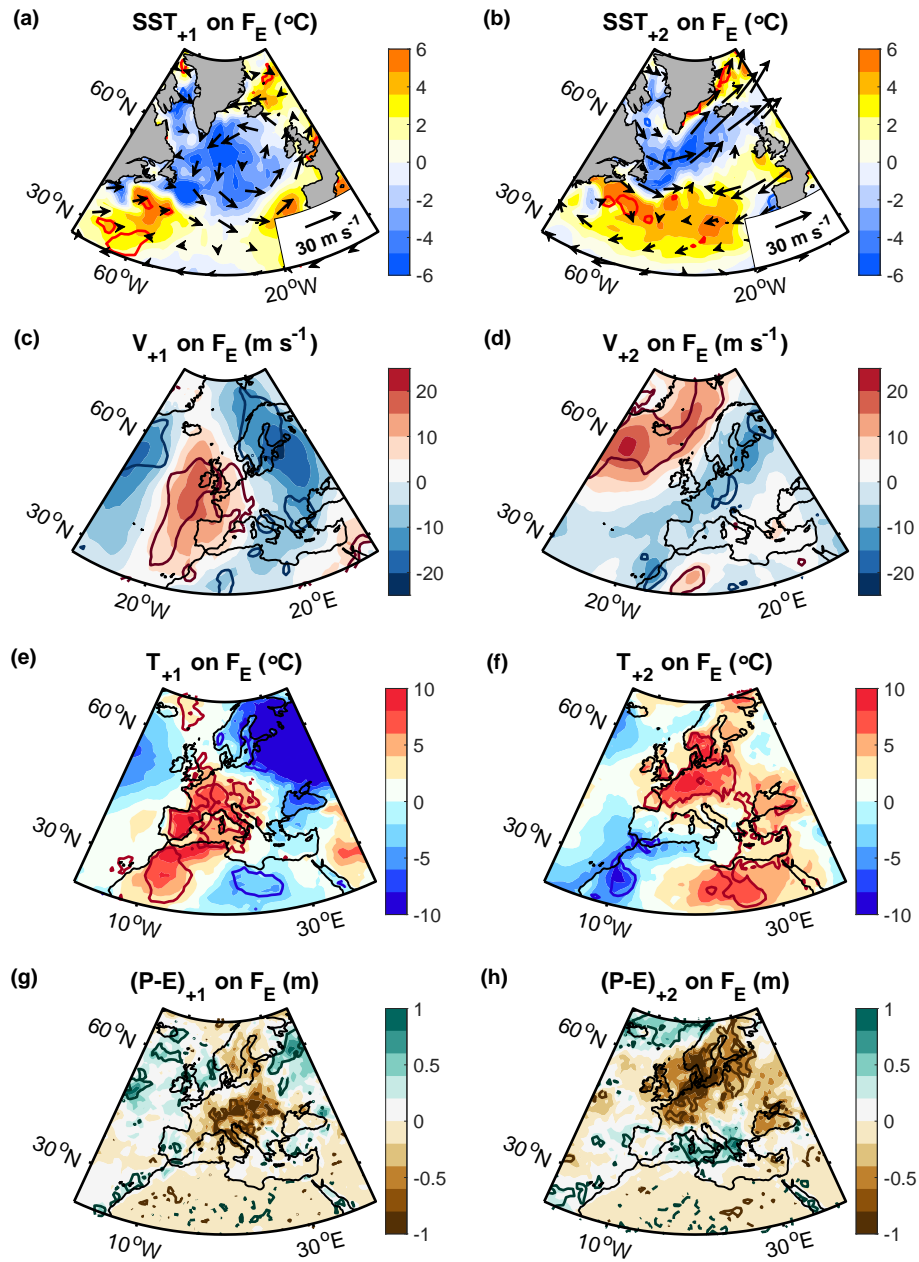
**Figure B1.** As in Figure 5 of the main manuscript, but with the NAO$_S$ index in 2019 included in the F$_E$ subset.
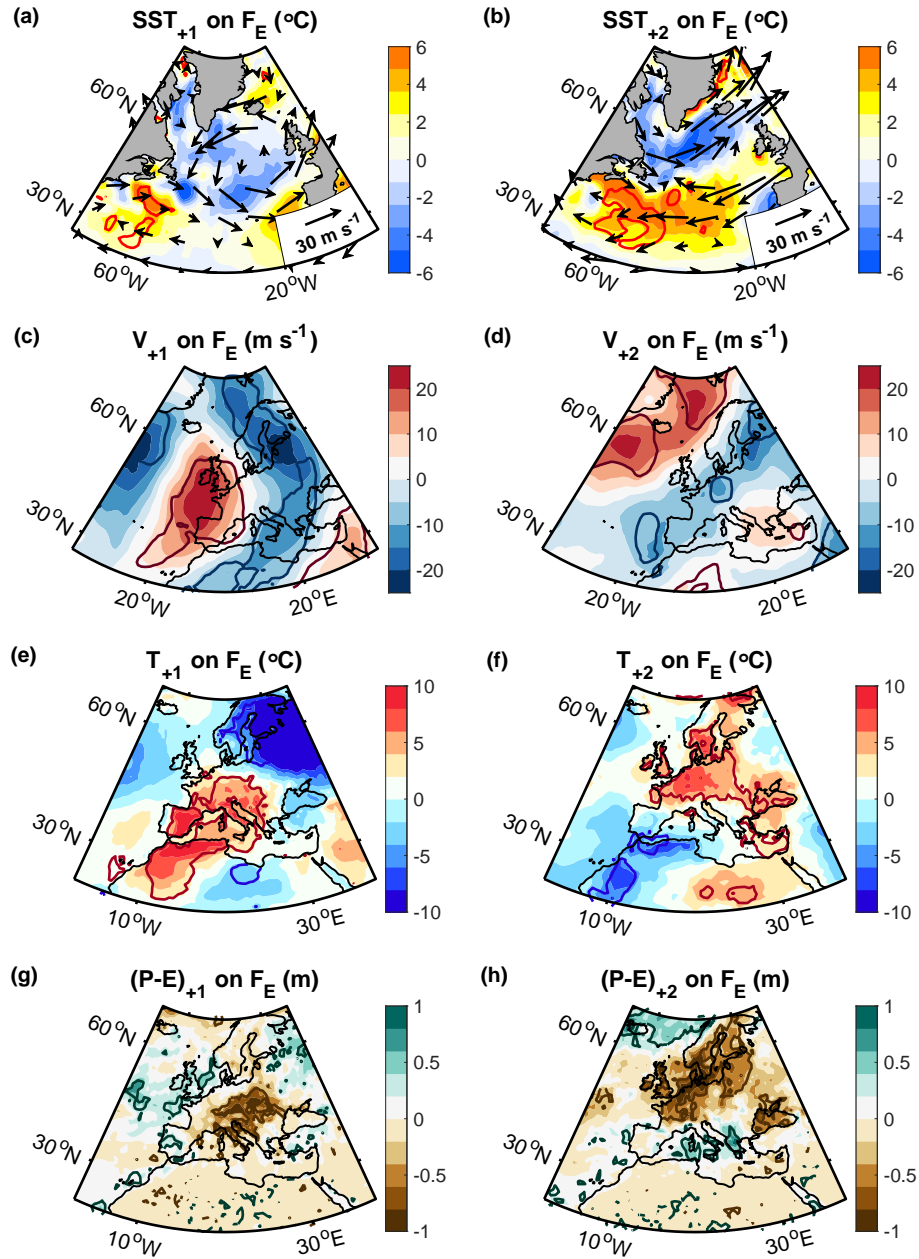
**Figure B2.** As in Figure 5 of the main manuscript, but excluding all consecutive years. Specifically, we only included the second year in all consecutive years. Thus, the regression is based on the $NAO_S$ years 1980, 1993, 2009, 2012 and 2016.
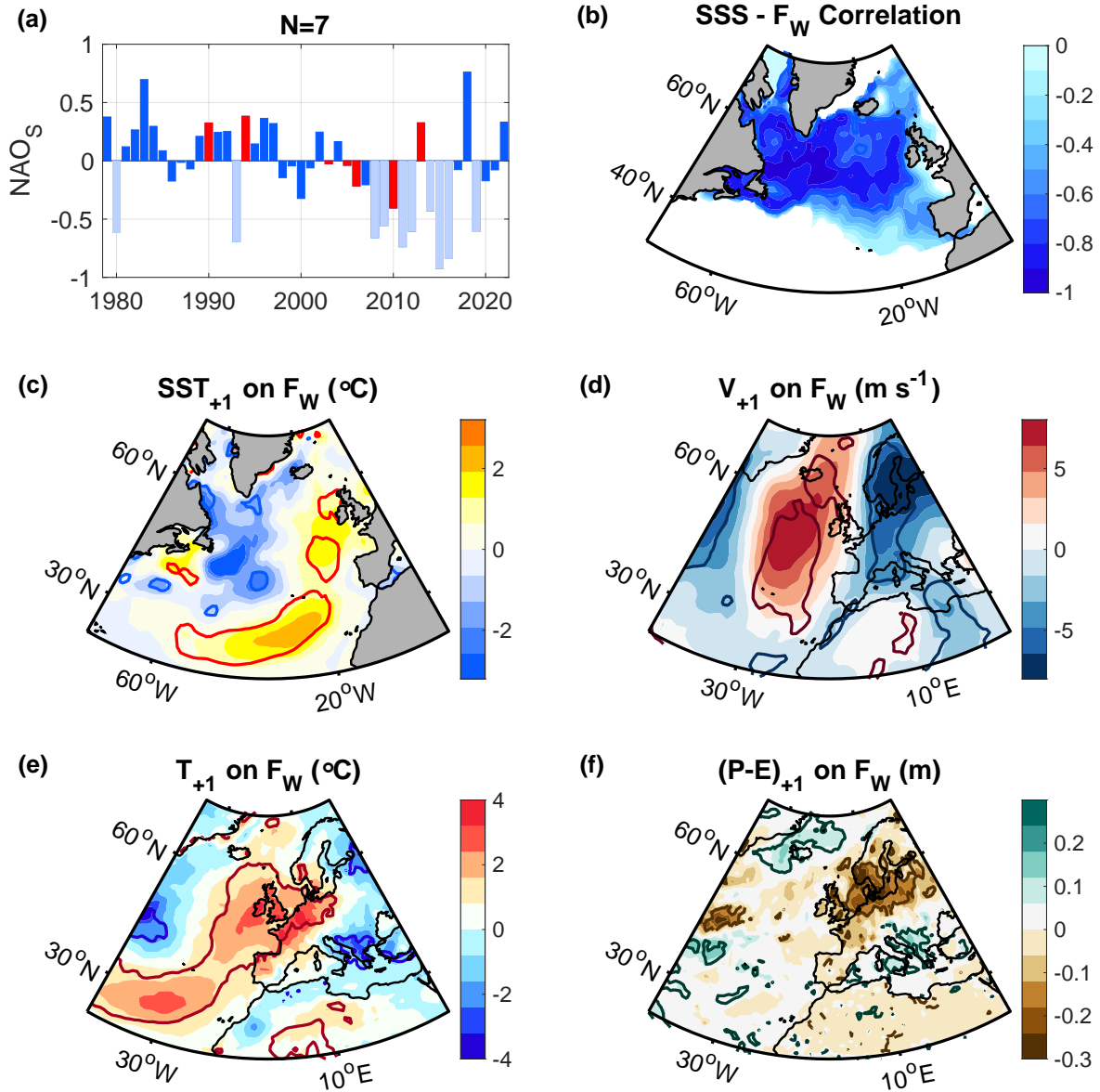
**Figure B3.** (a) $NAO_S$ index with the years included in the $F_W$ subset shown in red. Years excluded prior to the subsampling (including the 8 $F_E$ years and the two outliers) are shown as faint blue bars. (b) Correlation between the $F_W$ subset (the red $NAO_S$ years in panel a) and the associated SSS anomaly in the subsequent winter (January to March), estimated from the surface mass balance by assuming density compensation. (c-f) Regressions as in Figure 6 of the manuscript but including only 7 years in the $F_W$ subset (shown in panel a). The thick contours encompass regions that are significant at the 95% confidence level.
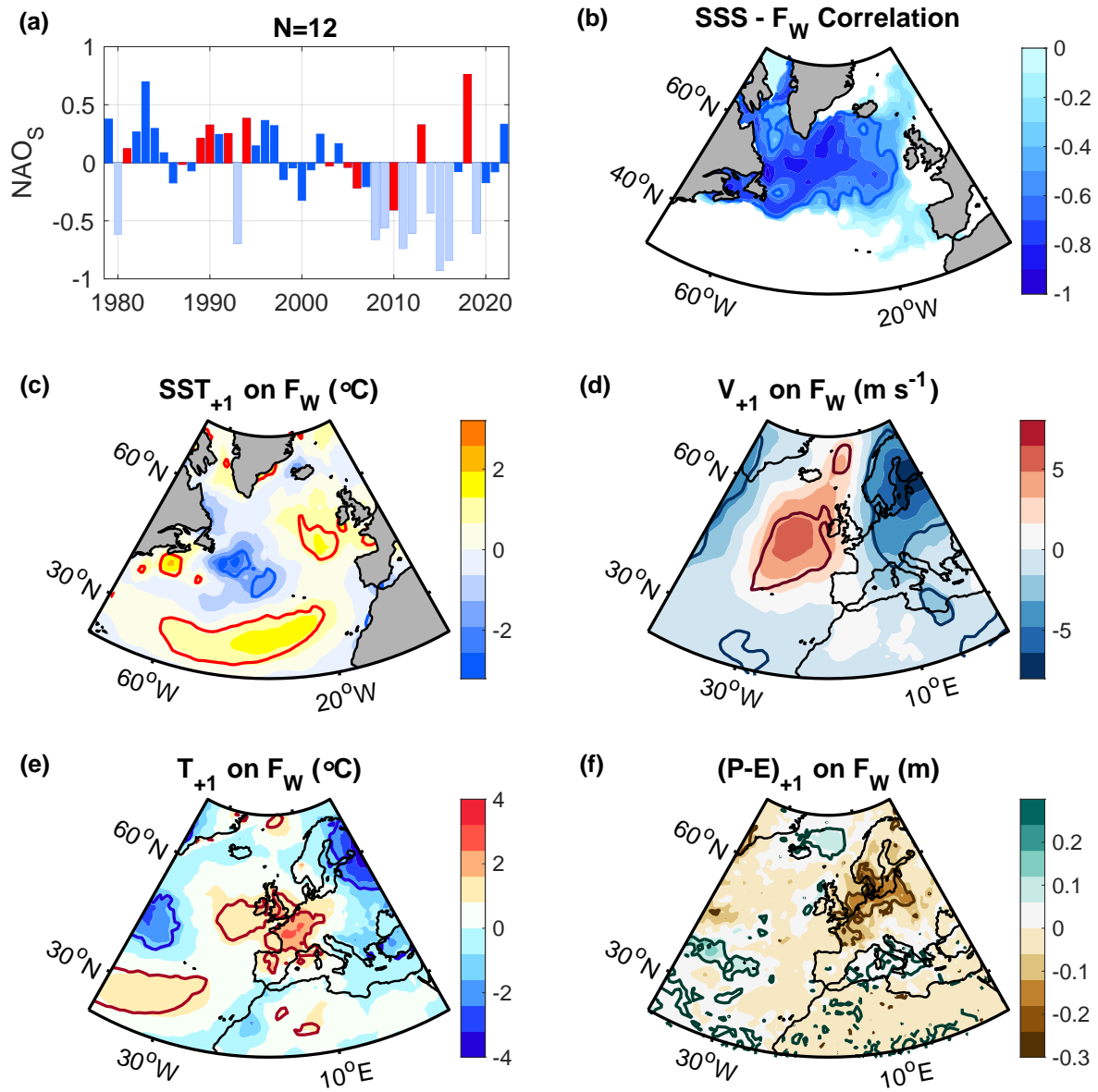
**Figure B4.** As in Figure B3 but for $N = 12$ years.
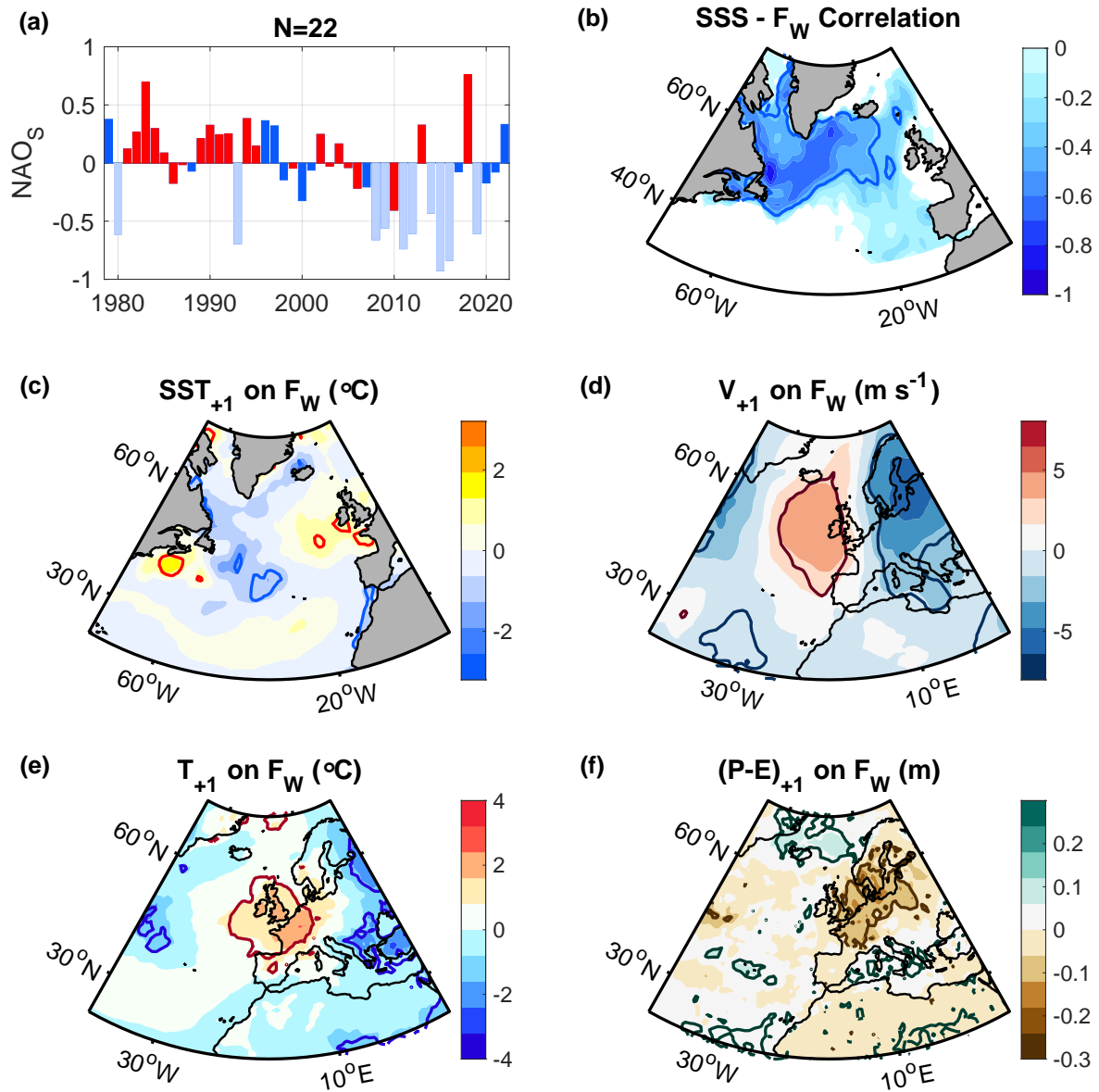
**Figure B5.** As in Figure B3 but for $N = 22$ years.
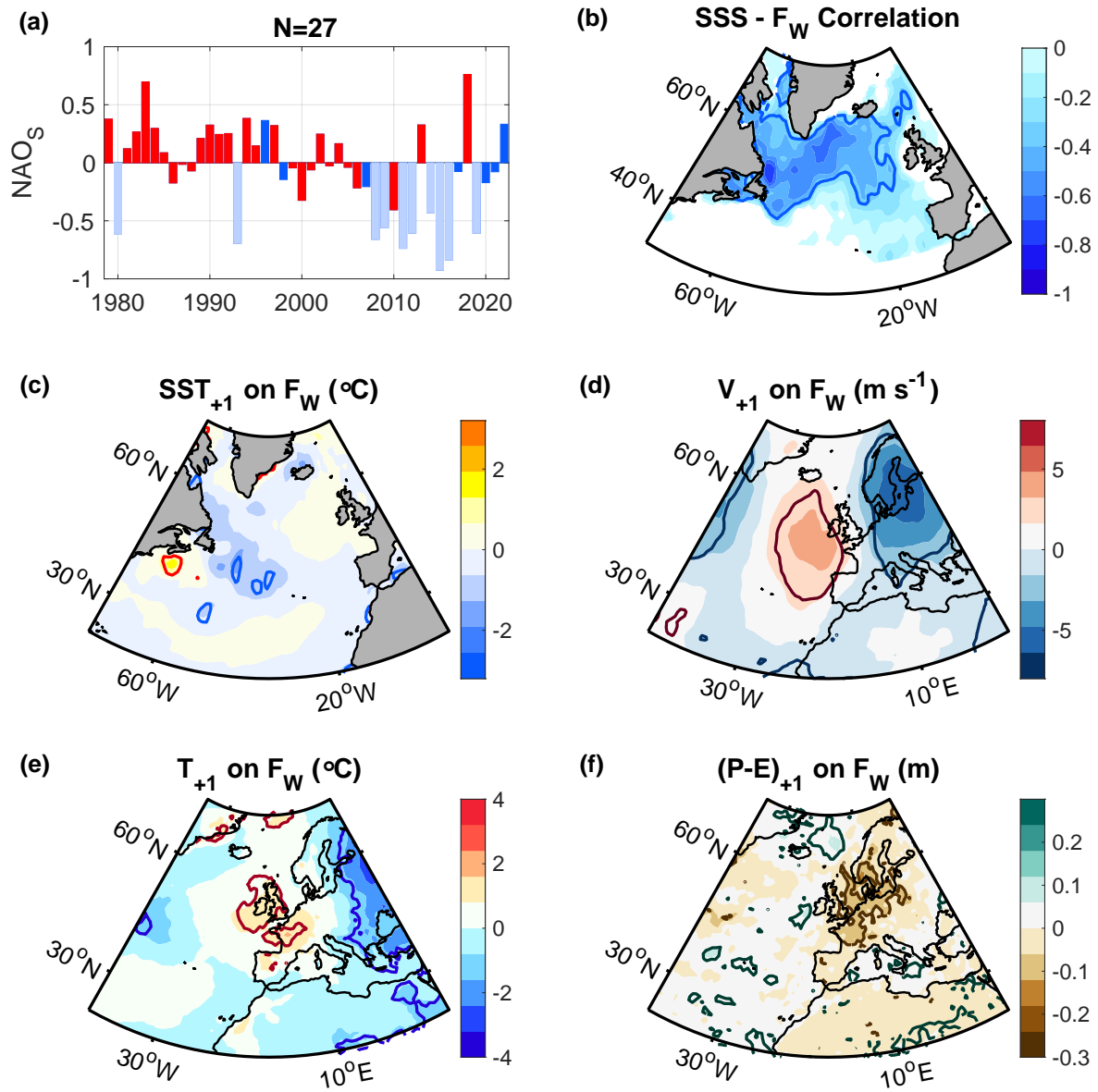
**Figure B6.** As in Figure B3 but for $N = 27$ years.
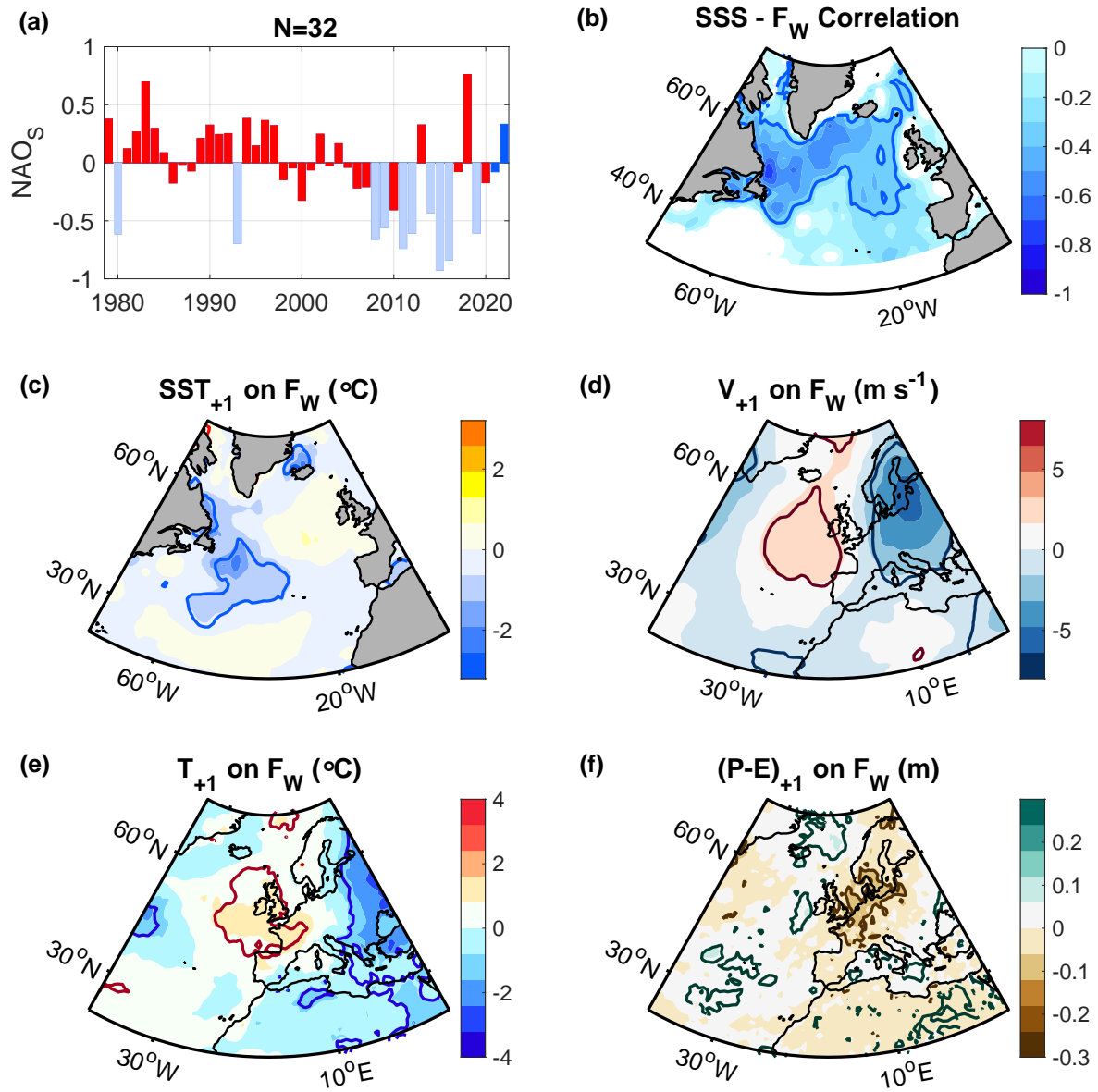
**Figure B7.** As in Figure B3 but for $N = 32$ years.

summer months (July and August). The filter does not include any other months. Thus, we lowpass filter the SST, winds at 700 hPa, the 2-m air temperature and precipitation minus evaporation variability with a 3-summer hanning filter. After the filtering, the resulting autocorrelations of European summer weather are still smaller than the one for the $\Delta$SST index. Nonetheless, we estimate the number of degrees of freedom based on the $\Delta$SST index, resulting in $N^* = \frac{N\Delta t}{2T_e} - 2$ degrees of freedom, where $N$ here is the number of data points, $\Delta t$ is the time interval between them, and $T_e$ is the e-folding timescale of the autocorrelations (Leith, 1973), which is 2 years for the $\Delta$SST index (Fig. 8a). While the regressions remain significant, their amplitude weakens (Fig. B8), indicating that the interannual variability, which has been filtered out, must have contributed to the increased relationship in the regressions obtained from the unfiltered time series (Fig. 7).
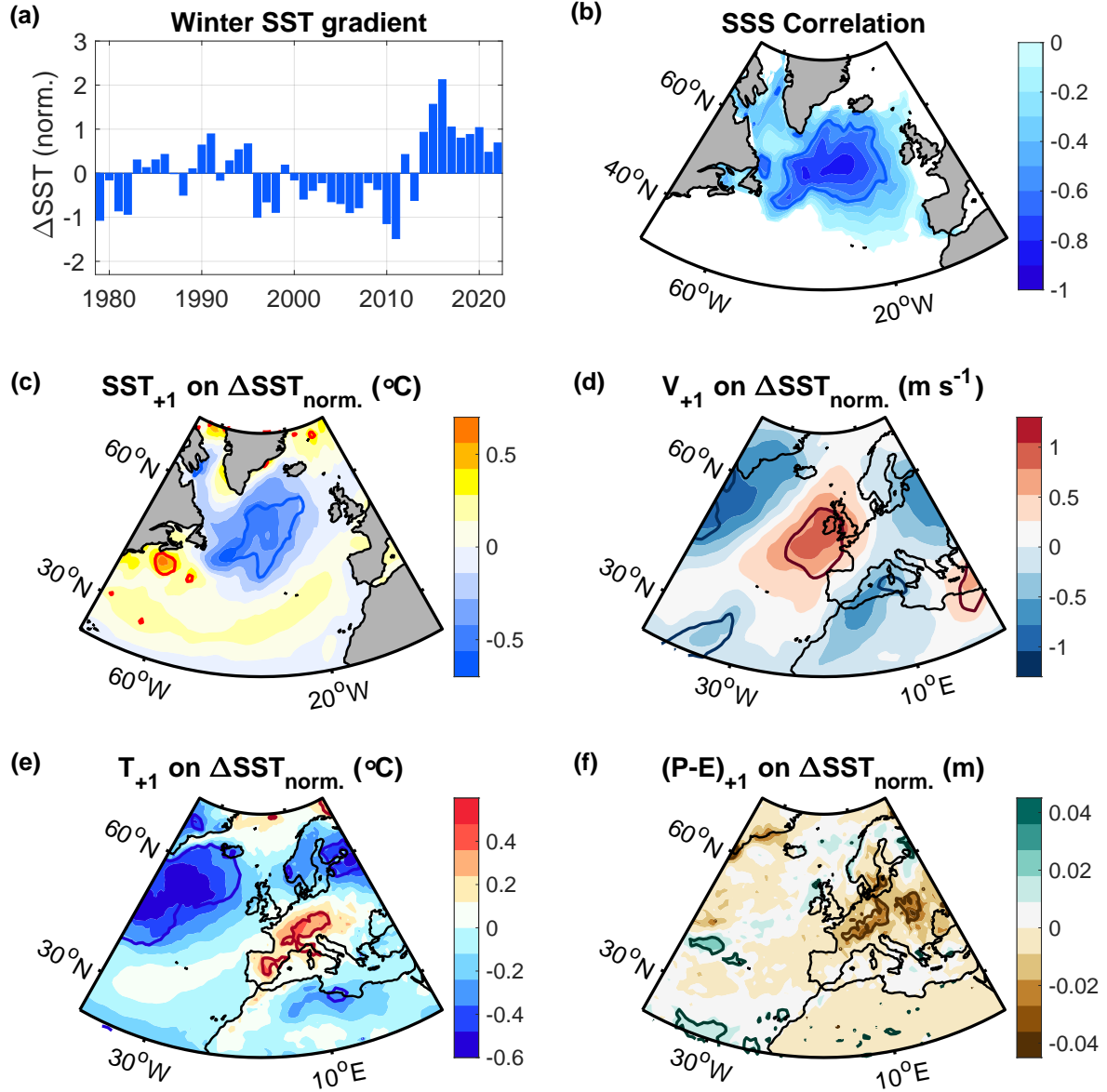
**Figure B8.** As in Figure 7 of the manuscript, after lowpass filtering the SST in summer (July and August), the 700 hPa winds in summer, and the 2-m air temperature and precipitation minus evaporation anomalies in summer, with a 3-summer hanning filter. The total number of degrees of freedom in the significance tests in all panels was estimated with $\frac{N\Delta t}{2T_e} - 2 = 9$, where $N$ is the number of years (which is 44), $\Delta t$ is one year, and $T_e$ is the lag where the correlation drops to the e-folding value ($\sim$0.37), corresponding to $\sim$2 years for the $\Delta$SST index.

**Table A1.** List of years included in the three freshwater indices $F_E$, $F_W$ and $\Delta$SST. The years listed for $F_E$ and $F_W$ correspond to the years of the summer NAO index in July and August, while the period listed for $\Delta$SST corresponds to the years of the SST anomalies in winter (January to March).

| $F_E$ | $F_W$ | $\Delta$SST |
|---|---|---|
| 1980 | 1981 | 1979 – 2022 |
| 1993 | 1982 | |
| 2008 | 1984 | |
| 2009 | 1987 | |
| 2011 | 1989 | |
| 2012 | 1990 | |
| 2015 | 1991 | |
| 2016 | 1992 | |
| | 1994 | |
| | 1995 | |
| | 2003 | |
| | 2004 | |
| | 2005 | |
| | 2006 | |
| | 2010 | |
| | 2013 | |
| | 2018 | |

*Author contributions.* M.O. conceived the study, carried out the analyses and was lead writer of the text. P.H. facilitated the implementation of the study; J.S. provided guidance in the model analysis; S.B. helped to revise the paper.

*Competing interests.* The authors declare that they have no conflict of interest.

*Acknowledgements.* We thank NOAA/OAR/ESRL and the Hadley Centre for providing the SST data, the Copernicus Marine Service for distributing the altimetry products, the European Centre for Medium-Range Weather Forecasts for developing the reanalysis ERA5 product, and the NOAA Physical Sciences Laboratory for facilitating access to the climate model outputs. We also thank Xavier Fettweis for providing output from the Greenland climate model MAR. The Argo data were collected and made freely available by the international Argo project and the national programs that contribute to it (http://doi.org/10.17882/42182). This study was funded through the grants ACSIS (NE/N018044/1), CLASS (NE/R015953/1) and CANARI (NE/W004984/1) from the UK National Environmental Research Council.

# References

Amos, D. E. and Koopmans, L. H.: Tables of the distribution of the coefficient of coherence for stationary bivariate Gaussian processes, vol. 483, Sandia Corporation, 1963.

Arribas, A., Glover, M., Maidens, A., Peterson, K., Gordon, M., MacLachlan, C., Graham, R., Fereday, D., Camp, J., Scaife, A., et al.: The GloSea4 ensemble prediction system for seasonal forecasting, Monthly Weather Review, 139, 1891–1910, 2011.

Bamber, J., van den Broeke, M., Ettema, J., Lenaerts, J., and Rignot, E.: Recent large increases in freshwater fluxes from Greenland into the North Atlantic, Geophysical Research Letters, 39, 2012.

Bamber, J., Tedstone, A., King, M., Howat, I., Enderlin, E., van den Broeke, M., and Noel, B.: Land ice freshwater budget of the Arctic and North Atlantic Oceans: 1. Data, methods, and results, Journal of Geophysical Research: Oceans, 123, 1827–1837, 2018.

Bao, S., Wang, H., Zhang, R., Yan, H., and Chen, J.: Comparison of satellite-derived sea surface salinity products from SMOS, Aquarius, and SMAP, Journal of Geophysical Research: Oceans, 124, 1932–1944, 2019.

Barnes, E. A.: Revisiting the evidence linking Arctic amplification to extreme weather in midlatitudes, Geophysical research letters, 40, 4734–4739, 2013.

Barnston, A. G. and Livezey, R. E.: Classification, seasonality and persistence of low-frequency atmospheric circulation patterns, Monthly weather review, 115, 1083–1126, 1987.

Blackport, R. and Screen, J. A.: Insignificant effect of Arctic amplification on the amplitude of midlatitude atmospheric waves, Science advances, 6, eaay2880, 2020.

Böning, C. W., Behrens, E., Biastoch, A., Getzlaff, K., and Bamber, J. L.: Emerging impact of Greenland meltwater on deepwater formation in the North Atlantic Ocean, Nature Geoscience, 9, 523–527, 2016.

Booth, J. F., Naud, C. M., and Willison, J.: Evaluation of extratropical cyclone precipitation in the North Atlantic basin: An analysis of ERA-Interim, WRF, and two CMIP5 models, Journal of Climate, 31, 2345–2360, 2018.

Briner, J. P., Cuzzone, J. K., Badgeley, J. A., Young, N. E., Steig, E. J., Morlighem, M., Schlegel, N.-J., Hakim, G. J., Schaefer, J. M., Johnson, J. V., et al.: Rate of mass loss from the Greenland Ice Sheet will exceed Holocene values this century, Nature, 586, 70–74, 2020.

Carmack, E. C., Yamamoto-Kawai, M., Haine, T. W., Bacon, S., Bluhm, B. A., Lique, C., Melling, H., Polyakov, I. V., Straneo, F., Timmermans, M.-L., et al.: Freshwater and its role in the Arctic Marine System: Sources, disposition, storage, export, and physical and biogeochemical consequences in the Arctic and global oceans, Journal of Geophysical Research: Biogeosciences, 121, 675–717, 2016.

Cohen, J., Screen, J. A., Furtado, J. C., Barlow, M., Whittleston, D., Coumou, D., Francis, J., Dethloff, K., Entekhabi, D., Overland, J., et al.: Recent Arctic amplification and extreme mid-latitude weather, Nature geoscience, 7, 627–637, 2014.

Cohen, J., Zhang, X., Francis, J., Jung, T., Kwok, R., Overland, J., Ballinger, T., Bhatt, U., Chen, H., Coumou, D., et al.: Divergent consensuses on Arctic amplification influence on midlatitude severe winter weather, Nature Climate Change, pp. 1–10, 2019.

Czaja, A. and Frankignoul, C.: Observed impact of Atlantic SST anomalies on the North Atlantic Oscillation, Journal of Climate, 15, 606–623, 2002.

Dierer, S., Schluenzen, K. H., et al.: Influence parameters for a polar mesocyclone development, METEOROLOGISCHE ZEITSCHRIFT-BERLIN-, 14, 781, 2005.

Dong, B., Sutton, R. T., Woollings, T., and Hodges, K.: Variability of the North Atlantic summer storm track: Mechanisms and impacts on European climate, Environmental Research Letters, 8, 034 037, 2013.

Duchez, A., Frajka-Williams, E., Josey, S. A., Evans, D. G., Grist, J. P., Marsh, R., McCarthy, G. D., Sinha, B., Berry, D. I., and Hirschi, J. J.: Drivers of exceptionally cold North Atlantic Ocean temperatures and their link to the 2015 European heat wave, Environmental Research Letters, 11, 074 004, 2016.

Dukhovskoy, D., Yashayaev, I., Proshutinsky, A., Bamber, J., Bashmachnikov, I., Chassignet, E., Lee, C., and Tedstone, A.: Role of Greenland freshwater anomaly in the recent freshening of the subpolar North Atlantic, Journal of Geophysical Research: Oceans, 124, 3333–3360, 2019.

Dunstone, N., Smith, D., Scaife, A., Hermanson, L., Fereday, D., O'Reilly, C., Stirling, A., Eade, R., Gordon, M., MacLachlan, C., et al.: Skilful seasonal predictions of summer European rainfall, Geophysical Research Letters, 45, 3246–3254, 2018.

Ferrari, R. and Wunsch, C.: Ocean circulation kinetic energy: Reservoirs, sources, and sinks, Annual Review of Fluid Mechanics, 41, 253–282, 2009.

Fettweis, X., Box, J. E., Agosta, C., Amory, C., Kittel, C., Lang, C., van As, D., Machguth, H., and Gallée, H.: Reconstructions of the 1900–2015 Greenland ice sheet surface mass balance using the regional climate MAR model, The Cryosphere, 11, 1015–1033, 2017.

Francis, J. A. and Vavrus, S. J.: Evidence linking Arctic amplification to extreme weather in mid-latitudes, Geophysical research letters, 39, 2012.

Fratantoni, P. S. and McCartney, M. S.: Freshwater export from the Labrador Current to the North Atlantic Current at the Tail of the Grand Banks of Newfoundland, Deep Sea Research Part I: Oceanographic Research Papers, 57, 258–283, 2010.

Gervais, M., Shaman, J., and Kushnir, Y.: Impact of the North Atlantic Warming Hole on Sensible Weather, Journal of Climate, 33, 4255–4271, 2020.

Gill, A. E.: Atmosphere—ocean dynamics, Elsevier, 2016.

Griffies, S. M. and Greatbatch, R. J.: Physical processes that impact the evolution of global mean sea level in ocean climate models, Ocean Modelling, 51, 37–72, 2012.

Häkkinen, S. and Rhines, P. B.: Shifting surface currents in the northern North Atlantic Ocean, Journal of Geophysical Research: Oceans, 114, 2009.

Häkkinen, S., Rhines, P. B., and Worthen, D. L.: Warm and saline events embedded in the meridional circulation of the northern North Atlantic, Journal of Geophysical Research: Oceans, 116, 2011a.

Häkkinen, S., Rhines, P. B., and Worthen, D. L.: Atmospheric blocking and Atlantic multidecadal ocean variability, Science, 334, 655–659, 2011b.

Häkkinen, S., Rhines, P. B., and Worthen, D. L.: Northern North Atlantic sea surface height and ocean heat content variability, Journal of Geophysical Research: Oceans, 118, 3670–3678, 2013.

Hanna, E., Jones, J. M., Cappelen, J., Mernild, S. H., Wood, L., Steffen, K., and Huybrechts, P.: The influence of North Atlantic atmospheric and oceanic forcing effects on 1900–2010 Greenland summer climate and ice melt/runoff, International Journal of Climatology, 33, 862–880, 2013.

Hanna, E., Cappelen, J., Fettweis, X., Mernild, S. H., Mote, T. L., Mottram, R., Steffen, K., Ballinger, T. J., and Hall, R. J.: Greenland surface air temperature changes from 1981 to 2019 and implications for ice-sheet melt and mass-balance change, International Journal of Climatology, 41, E1336–E1352, 2021.

Hátún, H., Sandø, A. B., Drange, H., Hansen, B., and Valdimarsson, H.: Influence of the Atlantic subpolar gyre on the thermohaline circulation, Science, 309, 1841–1844, 2005.

Hersbach, H., Bell, B., Berrisford, P., Biavati, G., Horányi, A., Muñoz Sabater, J., Nicolas, J., Peubey, C., Radu, R., Rozum, I., et al.: ERA5 hourly data on single levels from 1979 to present, Copernicus Climate Change Service (C3S) Climate Data Store (CDS), 10, 2018.

Heuzé, C.: North Atlantic deep water formation and AMOC in CMIP5 models, Ocean Science, 13, 609, 2017.

Holliday, N. P., Bersch, M., Berx, B., Chafik, L., Cunningham, S., Florindo-López, C., Hátún, H., Johns, W., Josey, S. A., Larsen, K. M. H., et al.: Ocean circulation causes the largest freshening event for 120 years in eastern subpolar North Atlantic, Nature Communications, 11, 1–15, 2020.

Holte, J., Talley, L. D., Gilson, J., and Roemmich, D.: An Argo mixed layer climatology and database, Geophysical Research Letters, 44, 5618–5626, 2017.

Hurrell, J. W., Hack, J. J., Shea, D., Caron, J. M., and Rosinski, J.: A new sea surface temperature and sea ice boundary dataset for the Community Atmosphere Model, Journal of Climate, 21, 5145–5153, 2008.

Khan, S. A., Aschwanden, A., Bjørk, A. A., Wahr, J., Kjeldsen, K. K., and Kjaer, K. H.: Greenland ice sheet mass balance: a review, Reports on progress in physics, 78, 046 801, 2015.

Kodama, C., Stevens, B., Mauritsen, T., Seiki, T., and Satoh, M.: A new perspective for future precipitation change from intense extratropical cyclones, Geophysical Research Letters, 46, 12 435–12 444, 2019.

Kostov, Y., Johnson, H. L., Marshall, D. P., Heimbach, P., Forget, G., Holliday, N. P., Lozier, M. S., Li, F., Pillar, H. R., and Smith, T.: Distinct sources of interannual subtropical and subpolar Atlantic overturning variability, Nature Geoscience, 14, 491–495, 2021.

Koul, V., Tesdal, J.-E., Bersch, M., Hátún, H., Brune, S., Borchert, L., Haak, H., Schrum, C., and Baehr, J.: Unraveling the choice of the north Atlantic subpolar gyre index, Scientific reports, 10, 1–12, 2020.

Kumar, A., Yadav, J., and Mohan, R.: Global warming leading to alarming recession of the Arctic sea-ice cover: Insights from remote sensing observations and model reanalysis, Heliyon, 6, e04 355, 2020.

Lashof, D. A. and Ahuja, D. R.: Relative contributions of greenhouse gas emissions to global warming, Nature, 344, 529–531, 1990.

Le Traon, P., Nadal, F., and Ducet, N.: An improved mapping method of multisatellite altimeter data, Journal of atmospheric and oceanic technology, 15, 522–534, 1998.

Leith, C.: The standard error of time-average estimates of climatic means, Journal of Applied Meteorology (1962-1982), pp. 1066–1069, 1973.

Lindzen, R. and Farrell, B.: A simple approximate result for the maximum growth rate of baroclinic instabilities, Journal of the atmospheric sciences, 37, 1648–1654, 1980.

Liu, W., Xie, S.-P., Liu, Z., and Zhu, J.: Overlooked possibility of a collapsed Atlantic Meridional Overturning Circulation in warming climate, Science Advances, 3, e1601 666, 2017.

Marshall, J., Johnson, H., and Goodman, J.: A study of the interaction of the North Atlantic Oscillation with ocean circulation, Journal of Climate, 14, 1399–1421, 2001.

Marzocchi, A., Hirschi, J. J.-M., Holliday, N. P., Cunningham, S. A., Blaker, A. T., and Coward, A. C.: The North Atlantic subpolar circulation in an eddy-resolving global ocean model, Journal of Marine Systems, 142, 126–143, 2015.

McDougall, T., Feistel, R., Millero, F., Jackett, D., Wright, D., King, B., Marion, G., Chen, C., Spitzer, P., and Seitz, S.: The international thermodynamic equation of seawater 2010 (TEOS-10): Calculation and use of thermodynamic properties, Global ship-based repeat hydrography manual, IOCCP report no, 14, 2009.

Mecking, J., Drijfhout, S., Jackson, L., and Andrews, M.: The effect of model bias on Atlantic freshwater transport and implications for AMOC bi-stability, Tellus A: Dynamic Meteorology and Oceanography, 69, 1299 910, 2017.

Mecking, J., Drijfhout, S., Hirschi, J. J., and Blaker, A.: Ocean and atmosphere influence on the 2015 European heatwave, Environmental Research Letters, 14, 114 035, 2019.

Menary, M. B., Hodson, D. L., Robson, J. I., Sutton, R. T., Wood, R. A., and Hunt, J. A.: Exploring the impact of CMIP5 model biases on the simulation of North Atlantic decadal variability, Geophysical Research Letters, 42, 5926–5934, 2015.

Müller, V., Kieke, D., Myers, P. G., Pennelly, C., Steinfeldt, R., and Stendardo, I.: Heat and freshwater transport by mesoscale eddies in the southern subpolar North Atlantic, Journal of Geophysical Research: Oceans, 124, 5565–5585, 2019.

Notz, D. and Stroeve, J.: The trajectory towards a seasonally ice-free Arctic ocean, Current climate change reports, 4, 407–416, 2018.

Oltmanns, M., Karstensen, J., Moore, G., and Josey, S. A.: Rapid cooling and increased storminess triggered by freshwater in the North Atlantic, Geophysical Research Letters, p. e2020GL087207, 2020.

Overland, J., Francis, J. A., Hall, R., Hanna, E., Kim, S.-J., and Vihma, T.: The melting Arctic and midlatitude weather patterns: Are they connected?, Journal of Climate, 28, 7917–7932, 2015.

Piron, A., Thierry, V., Mercier, H., and Caniaux, G.: Gyre-scale deep convection in the subpolar North Atlantic Ocean during winter 2014–2015, Geophysical Research Letters, 44, 1439–1447, 2017.

Priestley, M.: Spectral analysis and time series, number v. 1-2 in Probability and mathematical statistics, Academic Press, 86, 328, 1982.

Rayner, N., Parker, D. E., Horton, E., Folland, C. K., Alexander, L. V., Rowell, D., Kent, E., and Kaplan, A.: Global analyses of sea surface temperature, sea ice, and night marine air temperature since the late nineteenth century, Journal of Geophysical Research: Atmospheres, 108, 2003.

Reuter, M., Buchwitz, M., Schneising, O., Noël, S., Bovensmann, H., Burrows, J. P., Boesch, H., Di Noia, A., Anand, J., Parker, R. J., et al.: Ensemble-based satellite-derived carbon dioxide and methane column-averaged dry-air mole fraction data sets (2003–2018) for carbon and climate applications, Atmospheric Measurement Techniques, 13, 789–819, 2020.

Reynolds, R. W., Rayner, N. A., Smith, T. M., Stokes, D. C., and Wang, W.: An improved in situ and satellite SST analysis for climate, Journal of climate, 15, 1609–1625, 2002.

Schmidt, S. and Send, U.: Origin and composition of seasonal Labrador Sea freshwater, Journal of Physical Oceanography, 37, 1445–1454, 2007.

Screen, J. A. and Simmonds, I.: Exploring links between Arctic amplification and mid-latitude weather, Geophysical Research Letters, 40, 959–964, 2013.

Sgubin, G., Swingedouw, D., Drijfhout, S., Mary, Y., and Bennabi, A.: Abrupt cooling over the North Atlantic in modern climate models, Nature Communications, 8, 14 375, 2017.

Simmons, A. J.: Trends in the tropospheric general circulation from 1979 to 2022, Weather and Climate Dynamics, 3, 777–809, 2022.

Spall, M. A. and Pickart, R. S.: Wind-driven recirculations and exchange in the Labrador and Irminger Seas, Journal of Physical Oceanography, 33, 1829–1845, 2003.

Talley, L. D.: Descriptive physical oceanography: an introduction, Academic press, 2011.

Tang, Q., Zhang, X., and Francis, J. A.: Extreme summer weather in northern mid-latitudes linked to a vanishing cryosphere, Nature Climate Change, 4, 45–50, 2014.

Tesdal, J.-E., Abernathey, R. P., Goes, J. I., Gordon, A. L., and Haine, T. W.: Salinity trends within the upper layers of the subpolar North Atlantic, Journal of Climate, 31, 2675–2698, 2018.

Timlin, M. S., Alexander, M. A., and Deser, C.: On the reemergence of North Atlantic SST anomalies, Journal of climate, 15, 2707–2712, 2002.

Woollings, T., Hannachi, A., and Hoskins, B.: Variability of the North Atlantic eddy-driven jet stream, Quarterly Journal of the Royal Meteorological Society, 136, 856–868, 2010.

Wu, Y., Park, T., Park, W., and Latif, M.: North Atlantic climate model bias influence on multiyear predictability, Earth and Planetary Science Letters, 481, 171–176, 2018.

Wunsch, C. and Ferrari, R.: Vertical mixing, energy, and the general circulation of the oceans, Annu. Rev. Fluid Mech., 36, 281–314, 2004.

Xie, J., Raj, R. P., Bertino, L., Samuelsen, A., and Wakamatsu, T.: Evaluation of Arctic Ocean surface salinities from the Soil Moisture and Ocean Salinity (SMOS) mission against a regional reanalysis and in situ data, Ocean Science, 15, 1191–1206, 2019.

Yashayaev, I. and Loder, J. W.: Further intensification of deep convection in the Labrador Sea in 2016, Geophysical Research Letters, 44, 1429–1438, 2017.

Yu, H., Screen, J. A., Hay, S., Catto, J. L., and Xu, M.: Winter Precipitation Responses to Projected Arctic Sea-Ice Loss and Global Ocean Warming and Their Opposing Influences over Northeast Atlantic region, Journal of Climate, pp. 1–33, 2023.

Zhao, J. and Johns, W.: Wind-forced interannual variability of the Atlantic Meridional Overturning Circulation at 26.5 N, Journal of Geophysical Research: Oceans, 119, 2403–2419, 2014.